

# The Lunar Reconnaissance Orbiter Mission – Six years of science and exploration at the Moon



J.W. Keller\*, N.E. Petro, R.R. Vondrak, the LRO team

NASA Goddard Space Flight Center, Greenbelt, MD 20771, USA

## ARTICLE INFO

### Article history:

Received 30 June 2015

Revised 17 November 2015

Accepted 21 November 2015

Available online 17 December 2015

### Keywords:

Moon

Moon, surface

Geological processes

## ABSTRACT

Since entering lunar orbit on June 23, 2009 the Lunar Reconnaissance Orbiter (LRO) has made comprehensive measurements of the Moon and its environment. The seven LRO instruments use a variety of primarily remote sensing techniques to obtain a unique set of observations. These measurements provide new information regarding the physical properties of the lunar surface, the lunar environment, and the location of volatiles and other resources. Scientific interpretation of these observations improves our understanding of the geologic history of the Moon, its current state, and what its history can tell us about the evolution of the Solar System. Scientific results from LRO observations overturned existing paradigms and deepened our appreciation of the complex nature of our nearest neighbor. This paper summarizes the capabilities, measurements, and some of the science and exploration results of the first six years of the LRO mission.

Published by Elsevier Inc.

## 1. Introduction

### 1.1. LRO history

The history of lunar science and exploration and the need for advanced remote sensing missions, such as LRO, have been summarized by Mendell (2010). LRO was initiated in 2004 as an Exploration Mission with the goal of identifying desirable safe landing sites for the return of humans to the Moon or future robotic missions as part of NASA's Exploration Systems Mission Directorate. In addition, LRO's objectives included the search for surface resources and the measurement of the lunar radiation environment. The instruments were selected competitively to accomplish these focused objectives (Vondrak et al., 2010).

LRO was launched on June 18, 2009 and entered lunar orbit on June 23, 2009. After spacecraft commissioning in lunar orbit, the Exploration Mission began on September 15, 2009 and was completed on September 15, 2010 when operational responsibility for LRO was transferred to NASA's Science Mission Directorate for a two-year Science Mission with a new set of science goals. Following successful completion of the initial Science Mission, the LRO

team successfully defined entirely new mission goals in biannual senior reviews that resulted in extension of the LRO Science Mission, which is now scheduled to continue until at least September 2016.

The dual role of LRO as an exploration and science mission has proven to be very successful. Here we highlight important advances in both realms, focusing on contributions across LRO's evolving objectives without attempting to be fully comprehensive. As the mission has progressed, the LRO spacecraft has been operated robustly to maximize its value to NASA. It is still working well with a long lifetime ahead. The LRO mission has successfully accomplished all its objectives during each mission phase and has yielded an incredible data return of more than 625 terabytes from its data releases. These data and data products are a durable legacy for future explorers and scientists.

### 1.2. Importance of LRO

LRO has provided technical innovations and made surprising discoveries that have changed our view of the Moon. The science and exploration measurements will be a legacy of LRO that will be extremely useful to generations of lunar scientists and explorers.

Some of the LRO technical innovations are:

- First deep space precision orbit determination by laser ranging from Earth.
- First global thermal mapping of a planetary body covering a full range of local times and seasons.

\* Corresponding author at: Code 691, NASA Goddard Space Flight Center, 8800 Greenbelt Road, Greenbelt, MD 20771, USA.

E-mail address: [John.W.Keller@nasa.gov](mailto:John.W.Keller@nasa.gov) (J.W. Keller).

- First bi-static radar imaging measurements from Earth to a planetary orbiter.
- First multi-beam laser altimeter system in space.
- More than five years of laser altimetric measurements yielding 8 billion topographic points, better than any other object in the Solar System.
- First collimated epithermal neutron detectors in space.
- First use of tissue-equivalent-plastic (TEP) in deep space radiation detectors.

Some of the LRO exploration and science results are:

- In polar shadowed regions found the coldest spots measured (below 30 K) in the Solar System.
- Discovered significant subsurface hydrogen deposits in regions cold enough for water ice to survive, as well as in additional hydrogen deposits in warmer areas where surface water ice is not thermally stable.
- Measured surprising amounts of several volatiles (e.g., CO, H<sub>2</sub>, and Hg) in the gaseous cloud released from Cabeus by the LCROSS impact.
- New (<5 years old) impact craters and were found to be widespread across the lunar surface, with a surprising abundance of related surface changes.
- Developed an improved catalogue of lunar craters larger than 20 km in diameter, thus providing constraints on the ancient impactor population that affected the inner Solar System.
- First radar measurements of the lunar farside.
- Improved the age dating of small landforms by using crater counts from the new high-resolution images.
- Discovered that the Moon is in a general state of relatively recent (<1 Ga) contraction.
- Characterized relatively young volcanic complexes, such as Ina, and revealed first direct evidence of the presence of highly silicic volcanic rocks on the Moon.
- Measured galactic cosmic ray interactions with the Moon during a period with the largest cosmic ray intensities observed during the space age.
- Mapped in detail the temperatures, UV reflectance, and near-surface hydrogen abundance of the Moon's polar cold traps.
- Created the first cosmic ray albedo proton map of the Moon.
- Made high-resolution images of robotic and human exploration sites that showed hardware, the tracks of the astronauts, and surface disturbances from landing and ascent.

### 1.3. Purpose and organization of this paper

Here we summarize the capabilities of the LRO spacecraft and science results of the LRO mission to this point. Instrument and spacecraft capabilities are described in [Section 2](#). [Section 3](#) describes the LRO operations and evolution of its orbit. The LRO exploration measurements are described in [Section 4](#). Highlights of the first six years of science accomplishments are summarized in [Section 5](#), support for future landed missions is described in [Section 6](#), and conclusions are summarized in [Section 7](#).

## 2. LRO capabilities

### 2.1. LRO measurements

The LRO instruments use multiple techniques to obtain a unique set of observations of the Moon and the lunar environment. These instruments, which were previously described in detail ([Chin et al., 2007](#); [Vondrak et al., 2010](#)), are:

- Lunar Orbiter Laser Altimeter (LOLA), PI, David Smith (NASA Goddard Space Flight Center, Greenbelt, MD): a system that splits a single laser pulse into five laser spots at 28 times per second to measure topography, slopes and roughness ([Smith et al., 2010](#)).
- Lunar Reconnaissance Orbiter Camera (LROC), PI, Mark Robinson (Arizona State University, Tempe, Arizona): consisting of two narrow-angle cameras (NAC) with a spatial resolution of 50 cm from an altitude of 50 km and an ultraviolet/visible wide-angle camera (WAC) for global imaging in seven color bands with 100 m resolution ([Robinson et al., 2010](#)).
- Lunar Exploration Neutron Detector (LEND), PI, Igor Mitrofanov (Institute for Space Research, and Federal Space Agency, Moscow): neutron albedo measurements in three energy bands for detection of subsurface hydrogen ([Mitrofanov et al., 2010a](#)).
- Diviner Lunar Radiometer Experiment (Diviner), PI, David Paige (University of California, Los Angeles, California): a nine-channel infrared radiometer to measure thermal state, rock abundance, and regolith composition ([Paige et al., 2010a](#)).
- Lyman Alpha Mapping Project (LAMP), PI, Kurt Retherford (Southwest Research Institute, San Antonio, Texas): a far ultraviolet imaging spectrometer to measure water frost in permanently shadowed regions and the components of the lunar exosphere ([Gladstone et al., 2010b](#)).
- Cosmic Ray Telescope for the Effects of Radiation (CRaTER), PI, Nathan Schwadron (University of New Hampshire, Durham, New Hampshire): an energetic particle detector system to measure galactic cosmic rays and solar energetic particle events ([Spence et al., 2010](#)).
- Miniature Radio-Frequency Technology Demonstration (Mini-RF), P.I. Wes Patterson (Applied Physics Laboratory, Laurel, Maryland): a synthetic aperture radar to measure regolith properties and search for subsurface ice ([Nozette et al., 2010](#)).

The instruments are shown and described in [Fig. 1](#) and [Table 1](#). Each LRO instrument has independent capabilities for providing both scientific and engineering-enabling measurements of the lunar surface and environment. Additionally, a key feature is that the instrument payload set makes complementary measurements that reinforce the discoveries of any individual instrument, so as to reduce ambiguity and to make as comprehensive a set of observations as possible ([Vondrak et al., 2010](#)). For example, surface features and hazards are measured by LROC, Mini-RF, and LOLA, while Diviner infers rock abundance from its temperature data. The search for water ice is accomplished by: LAMP and LOLA, which can measure surface frost; Mini-RF, which can detect near-surface rocky ice; and LEND, which is sensitive to hydrogen within a meter of the surface. As yet another example, the interiors of polar shadowed regions are revealed by LAMP (which uses both UV starlight and interplanetary Lyman-alpha sky-glow), LOLA (which makes high resolution topographic maps), Diviner (which makes infrared emission images), LROC (which uses secondary solar illumination), and Mini-RF (which makes radar images).

### 2.2. The LRO spacecraft

The LRO orbiter is a 3-axis stabilized spacecraft that is generally pointed in a nadir direction to allow continuous mapping of the lunar surface by the remote sensing instruments. The spacecraft is able to slew for instrument calibrations and specialized measurements, such as exospheric measurements and stereo imaging.

The locations of the instruments and major subsystems on the LRO spacecraft are shown in [Figs. 1](#) and [2](#). The LRO spacecraft bus is approximately 2 m tall. Its total mass is approximately 800 kg dry, and was 1700 kg when fully fueled.



**Fig. 1.** The LRO spacecraft in a Goddard Space Flight Center cleanroom is mounted on spin-test platform after being fully blanketed. The locations of the instruments are labeled and the solar panels, at right, are in their pre-launch stowed configuration. For scale the spacecraft is 2 m tall (see Fig. 2) [GSFC/Office of Communications].

LRO has a monopropellant hydrazine propulsion system used for capture into a polar orbit at the Moon and for later adjustment of its orbital parameters. Four reaction wheels provide attitude control and momentum storage, with hydrazine thrusters being used periodically for momentum unloading. Two star trackers and an inertial reference unit provide attitude knowledge. A 10.7 square meter solar array provides 2 kW during the sunlit portion of the orbit. Two 100-Gbyte recorders store science data for playback to Earth at 100 Mbps through a Ka-band transmitter. Other details of the LRO spacecraft capabilities and mission design are described in [Tooley et al. \(2010\)](#).

A unique feature of the LRO spacecraft is the precision orbit determination that is provided by one-way laser tracking of LRO from Earth-based laser ranging facilities, which is enabled by the LOLA instrument and significantly improves the vertical accuracy of the topographic measurements ([Zuber et al., 2010](#)).

### 3. LRO operations

Spacecraft and mission operations are based at the LRO Mission Operations Center (MOC) at NASA's Goddard Space Flight Center. The instrument operations are led by Science Operation Centers at the instrument institutions, which are also responsible for instrument data processing and data deliveries to the Planetary Data System. The LRO spacecraft has performed exceptionally for more than 5 years in lunar orbit with 98.4% uptime for lunar measurements. Only one-third of the downtime was due to spacecraft anomalies, with the remainder of the downtime due to thruster maneuvers, eclipses, and instrument calibration attitude slews, during which several or all instruments are turned off.

Over the more than six years of operations the MOC has developed new approaches to safely operating LRO, including simulation tools for evaluating the effects of slews and off nadir operations on momentum management, the thermal environment and power profile, while the orbit prediction and determination have been greatly improved in accuracy by use of the new GRAIL model of the lunar gravitational field.

#### 3.1. Orbit history

To provide a substantial capability to adjust its orbit, nearly half of the LRO spacecraft mass at launch was hydrazine fuel. The evolution of the LRO mission orbit is shown in Fig. 3. During its commissioning phase, LRO was initially placed into a  $30 \text{ km} \times 200 \text{ km}$  quasi-stable polar orbit with periselene over the south pole, an orbit that is relatively easy to maintain. Marking the beginning of the exploration phase of the mission, LRO on September 15, 2009 was moved to a quasi-circular mapping orbit, which was maintained at 50 km mean altitude with monthly station-keeping propulsive maneuvers. Without these station-keeping maneuvers, the LRO spacecraft would have impacted the surface in approximately 40 days. In August and November of 2011 the periselene was lowered to 21 km in order to obtain high resolution imaging of the Apollo landing sites and other locations of scientific interest. With diminishing fuel, on December 11, 2011 the LRO spacecraft was returned to the approximately  $30 \text{ km} \times 200 \text{ km}$  quasi-stable polar orbit, which can be maintained for at least seven years with the existing fuel reserves. Currently the orbit is adjusted with annual station-keeping propulsive maneuvers.

LRO was initially placed in a polar orbit in order to make global coverage and to allow repetitive measurements at high latitudes. Even though the tilt of the lunar spin axis with respect to the ecliptic plane is very small, only  $1.56^\circ$ , there are some seasonal variations in the illumination and resultant physical characteristics in the lunar polar region. For this reason the launch and orbital insertion was timed to assure that the LRO ground track was initially near local noon/midnight at the solstices when the seasonal extremes are expected, though this is no longer the case. Because of lunar orbital variations, the inclination of the orbital plane has moved to lower latitudes at the rate of approximately 0.5 degrees per year.

#### 3.2. Targeting/slews

During the Science Mission, the LRO spacecraft and instruments have been operated in innovative modes, with intensive campaigns and rapid response to new opportunities. The slewing rate has been made faster (from the initial 0.1 degrees per second to as much as 0.15 degrees per second), so as to facilitate more off-nadir observations each day (for example during co-incident LADEE observations, see below). Faster slews result in longer time on target during periods of limited power and thermal balance. Slews have many scientific benefits, including spectacular oblique images of lunar features. For example, Fig. 4 shows an oblique image of the central peak of the crater Tycho, one of the youngest large impact craters.

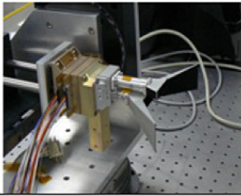
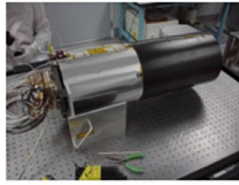
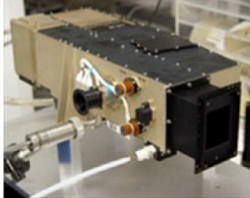
#### 3.3. Special events and campaigns

In addition to routine measurements, the LRO spacecraft team operates during special events, such as eclipses, spacecraft impacts (e.g. LCROSS, GRAIL), and in special observational campaigns.

During lunar eclipses the spacecraft must be operated carefully for thermal and power management. The position of LRO in its orbit is carefully adjusted to minimize the time in darkness. The spacecraft is preheated for several hours before the eclipse.

Table 1

LRO's suite of seven instruments measures a range of surface properties. Details from [Vondrak et al. \(2010\)](#).

|   |   |  |
|---|---|--|
| <p><b>LOLA: Lunar Orbiter Laser Altimeter</b></p> <ul style="list-style-type: none"> <li>- Topography</li> <li>- Slopes</li> <li>- Roughness</li> </ul> <p>5-spot altimeter<br/>10 cm vert.<br/>25 m horz.<br/>resolution</p>    | <p><b>LROC/WAC: Wide-Angle Camera</b></p> <ul style="list-style-type: none"> <li>- Global Imagery</li> <li>- Lighting</li> <li>- Resources</li> </ul> <p>7-band UV/Vis filters, ~100 m resolution from 50 km altitude</p>    | <p><b>LROC/NACs: Narrow-Angle Cameras</b></p> <ul style="list-style-type: none"> <li>- Targeted Imagery</li> <li>- Hazards</li> <li>- Topography</li> </ul> <p>50 cm resolution<br/>2 NACs with 5 km combined swath from 50 km</p>  |
| <p><b>LR: Laser Ranging</b></p> <ul style="list-style-type: none"> <li>- Precision Orbit Determination</li> </ul> <p>Uses LOLA detector to range from Earth to LRO</p>   | <p><b>Diviner Lunar Radiometer</b></p> <ul style="list-style-type: none"> <li>- Thermal State</li> <li>- Volatile Stability</li> <li>- Rocks&amp;Regolith</li> <li>- Composition</li> </ul> <p>0.35 to 400 <math>\mu\text{m}</math> in 9 channels<br/>~150-500 m res.</p>  | <p><b>Mini-RF: Synthetic Aperture Radar</b></p> <ul style="list-style-type: none"> <li>- Resources</li> <li>- Topography</li> <li>- Hazards</li> </ul> <p>Bistatic radar measurements<br/>30 m S &amp; X SAR imagery</p>            |
| <p><b>CRaTER: Cosmic Ray Telescope...</b></p> <ul style="list-style-type: none"> <li>- Radiation Spectra</li> <li>- Tissue Effects</li> </ul> <p>LET spectra<br/>Behind tissue<br/>Equiv. plastic<br/>0.9 keV/<math>\mu\text{m}</math> to 2.2 MeV/<math>\mu\text{m}</math></p>  | <p><b>LEND: Lunar Explr. Neutron Detector</b></p> <ul style="list-style-type: none"> <li>- Neutron Albedo</li> <li>- Hydrogen Maps</li> </ul> <p>Thermal, epithermal and energetic neutrons<br/>10 km spatial resolution from 50 km</p>                                   | <p><b>LAMP: Lyman-Alpha Mapping Project</b></p> <ul style="list-style-type: none"> <li>- Water-Frost</li> <li>- PSR Maps</li> </ul> <p>UV imaging<br/>57 to 196 nm<br/>0.18 nm spec. resolution<br/>~300 m spatial</p>             |

Instruments are generally turned off, except for the Diviner instrument, which makes targeted measurements of the regolith cooling rate during the eclipse (see [Section 5.3](#)). The capability to operate any of the instruments during eclipses was not a requirement. Only after it was demonstrated that the spacecraft batteries could support observations during periods of prolonged darkness did mission management clear Diviner to operate during eclipses.

A major event that occurred early during the LRO mission was the support of the Lunar Crater Observation and Sensing Satellite (LCROSS) impact in Cabeus crater on October 9, 2009 ([Colaprete et al., 2010](#)). When LRO was manifested on an Atlas V rocket, NASA took advantage of the additional lift capacity to launch LCROSS simultaneously with LRO. LRO made detailed observations before, during, and after the LCROSS impact at Cabeus crater near the lunar south pole ([Hayne et al., 2010](#); [Gladstone et al., 2010a](#)). During the commissioning phase LRO assisted LCROSS by detailed mapping of potential impact sites so as to select one that might be very cold and contain volatiles. The LRO orbit was adjusted to pass near the impact site soon after impact occurred enabling observation of the impact plume. Similarly, when the two Gravity Recovery and Interior Laboratory (GRAIL) spacecraft impacted a northern sunlit lunar mountain on December 17, 2012, LAMP observed the volatile impact cloud and LROC imaged the two craters that were formed ([Robinson et al., 2015](#)). The results from these observations are discussed below.

Several off-nadir observing campaigns are also used for special scientific measurements. For example, in coordination with the Lunar Atmosphere and Dust Environment Explorer (LADEE) mission, a LAMP exospheric campaign measured exospheric species with a frequent cadence at optimum observing times. Additional examples of focused campaigns are the use of the NAC in targeted campaigns for stereo measurements, as well as for re-imaging of previous sites to identify surface changes.

### 3.4. LRO data

A critical capability for LRO is its very high downlink data rate of 100 Mbps, which is enabled by both the proximity of the Moon to the Earth and the use of a dedicated telemetry ground station at White Sands, New Mexico.

The LRO data are added to NASA's Planetary Data System (PDS) at three-month intervals, with a latency of no more than six months. These include not only raw and calibrated data, but also higher-level data products, such as mosaics, derived surface parameters, and maps of geophysical quantities, all of which are archived within 6 months of their creation. The principal data products for each LRO instrument have been described in [Chin et al. \(2007\)](#) and in [Vondrak et al. \(2010\)](#). [Fig. 5](#) shows the LRO instrument data archive architecture and the relationship of each instrument Science Operation Center (SOC) to the PDS Nodes and Data Nodes. As of 15 September 2015, more than 625 terabytes of LRO measurements have been made available for use by scientists and the public.

The value of such an enormously large data volume that spans more than 6 years has been shown by LOLA's high resolution topographic grid spacing near the poles, reimagining for detection of recent impacts by LROC, measurement of lunar regolith photometric parameters at many illumination and observation angles, as well as the scientific benefits indicated in the sections below. No other Solar System body besides the Earth has such a large (by volume) data set. However, as laser communications result in high bandwidth capability for deep space missions, the example of LRO will be a pathfinder for data organization, analysis, and research topics. As a result of the wide range in data produced by the instrument teams, a number of web-based tools have been developed, both within and outside of the LRO teams, to navigate and work with the LRO data volume. The LROC team has produced

a number of web-based tools to search, view, and download their products. For example the QuickMap webpage (LROC Team et al., 2015) enables users to view global products as well as search for and download NAC images covering areas of interest.

### 3.5. Public engagement

The LRO teams have been extremely successful in communicating their results to educators, students, and the public through an effective Education and Public Outreach program. Especially effective has been the LRO leadership of the International Observe the Moon Night events (Bleacher et al., 2015), and the annual Lunar Workshops for Educators (Jones et al., 2015). Of particular interest to the public, as well as historians, have been the high-resolution LROC images of the Apollo landing sites (Fig. 6). They provide precise surface experiment locations, the fine-scale geologic context from which samples were collected, and the tracks of the astronauts. They document current physical conditions at these key locations, revealing the effects of human and robotic activity on the lunar surface and its degradation over time. A very effective method for communicating mission results to the public has been *via* videos and animations showcasing new data products and scientific findings. The LRO data visualizations and animations are available on the SVS site at GSFC (Jones et al., 2015).

## 4. LRO exploration products

The purpose of the initial one-year Exploration Mission was to acquire information and develop maps that would enable safe and efficient return to the Moon, as well as the identification of sites of greatest interest. Additional important objectives were the search for resources and the measurement of the space radiation that might be damaging to humans. All of these objectives were successfully accomplished.

### 4.1. Global and regional maps

During its primary Exploration Mission LRO data were used to develop global maps of many important lunar characteristics. A few examples of the products and associated publications are:

- Global 7-color image maps from LROC/WAC with a spatial resolution of 100 m (Denevi et al., 2014; Sato et al., 2014).
- Global temperature maps to better than 500 m spatial resolution by Diviner (Paige et al., 2010b; Bandfield et al., 2011).
- Global Mini-RF maps of roughness and radar scattering characteristics at a resolution of ~250 m for the upper meter of the lunar surface (Cahill et al., 2014).
- Global LOLA topography maps with 10 cm vertical resolution, 1 m vertical accuracy and 100 m horizontal resolution. After one year these maps had an average cross-track spacing at the equator of 1 km, which has subsequently been reduced to less than 200 m (Head et al., 2010).
- Global maps of surface slopes and roughness (see Fig. 7) (Kreslavsky et al., 2013; Rosenburg et al., 2011, 2015).
- Surface rock abundance map derived from surface temperature (Bandfield et al., 2011).
- Map of silicate mineralogy derived from the position of the Christiansen Feature (Greenhagen et al., 2010).
- Specially produced polar products:
  - Illumination conditions near the poles (Mazarico et al., 2011; Speyerer and Robinson, 2013).
  - High Resolution Polar Topographic Maps (Zuber et al., 2012)
  - Polar Temperature Products (Paige et al., 2010b).

### 4.2. Special regions

In addition to global maps, during the Exploration Mission detailed measurements were required for 50 lunar locations (Table 2 and Fig. 8) that had been selected as Constellation regions of interest or ROIs (Gruener and Joosten, 2009; Jolliff et al., 2010; Lawrence et al., 2010). These are special regions of interest because of their scientific importance or because they were representative examples of many other lunar locations that might be desirable landing sites for future robotic or human exploration missions. Geometric stereo coverage and controlled NAC mosaic coverage are generally comprehensive for these sites over an area of about 100 km<sup>2</sup>.

A primary objective of the Exploration Mission was the characterization of the lunar polar regions, which had not been measured well by previous missions. A special exploration objective was to search for resources there. These resources were expected to be both polar volatiles and also regions of near permanent illumination near the lunar poles. The search for evidence of volatiles such as water ice was successful and is described in detail in Section 5.1.

The measurement of illumination conditions was important because regions of persistent sunshine are candidate sites for robotic or human lunar outposts due to the persistent availability of sunlight for power and the relatively benign temperature conditions. At high latitudes the illumination is determined by the complex surface topography, with small seasonal variations due to the obliquity of the lunar spin axis. Two approaches have been used to determine illumination conditions in these regions. A direct approach is to image the changing lighting with LROC (Speyerer and Robinson, 2013). Another approach that has predictive capability is to calculate illumination from the high-resolution digital elevation model from LOLA. Mazarico et al. (2011) used these LOLA data to evaluate lighting conditions for several lunar precession periods and found many locations that are sunlit more than 85% of the time.

### 4.3. Effects of the lunar radiation environment on astronauts

Because a primary objective of the LRO exploration mission was to obtain information that could be used to estimate the effects of space radiation on astronauts in deep space, LRO has an innovative sensor of high-energy radiation, CRaTER. CRaTER uses tissue-equivalent plastic within a detector array to measure the biological effectiveness of the space radiation. It measures the protons, heavy ions, and neutrons that are a hazard to astronauts, and its data can be used to calculate doses, dose rates, organ doses, and the effectiveness of various shielding materials. A special issue of Space Weather is devoted specifically to the CRaTER measurements, and their long-ranging implications for human exploration and our understanding of the space environment (Schwadron et al., 2013).

There are three types of space radiation that are of concern to astronaut health: galactic cosmic rays (GCR), which were enhanced at solar minimum when LRO was launched, and solar particle events (SPE), which occurred sporadically later in the mission (Fig. 9), and radiation albedo, created from excited nuclei within the regolith and re-radiate from the lunar surface. The radiation albedo is particularly intense for neutrons (Looper et al., 2013), which have high quality factors and therefore strongly interact with biological systems.

Remarkably, LRO was launched at the deepest solar minimum during the entire space age, and has characterized the radiation impacts of the highest levels of galactic cosmic rays observed in more than 80 years. This characterization is critical in understanding how our space environment is changing (Schwadron et al., 2011),

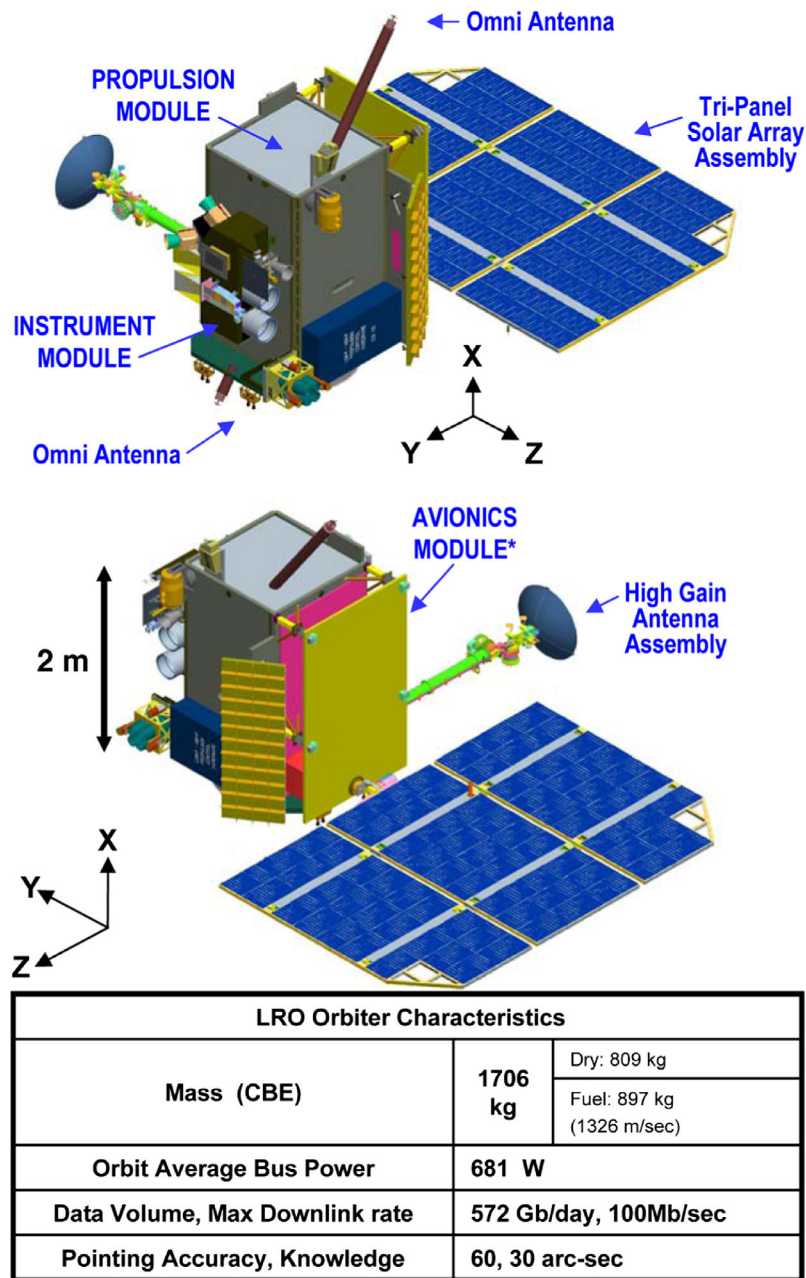


Fig. 2. Assembly level schematic of the LRO spacecraft showing antenna locations and propulsion systems, with a summary of its relevant specifications.

and what the impacts are for long-term human exploration (Schwadron et al., 2014).

### 5. LRO science objectives and accomplishments

In its first six years of operations, data from LRO has advanced lunar and Solar System science by enabling ground breaking discoveries. These discoveries challenge our understanding of the distribution and inventory of volatiles on the surface; reveal the Moon to have been volcanically active more recently than previously thought; that tectonics have modified the surface within the last several million years and may be actively modifying the surface today; demonstrated that the rate of contemporary impacts is possibly higher than anticipated; and provide a unprecedented understanding of the interactions of the Moon’s surface with the changing space environment.

The science objectives for the LRO Science Mission have addressed specific themes that have evolved during the mission. These themes and some of the science results are described below.

#### 5.1. Distribution and transport of volatiles

A primary objective of the LRO mission is to search for volatiles that might reside in the lunar polar regions, which had not been measured with sufficient spatial resolution by previous missions. The LRO observations have revolutionized our understanding of volatiles in these regions.

The possibility that significant water ice may be sequestered in the cold permanently shadowed regions (PSRs) of the Moon have intrigued scientists and explorers ever since it was first suggested by Watson et al. (1961) and Arnold (1979). Morgan and Shemansky (1991) suggested that water on the surface of PSRs

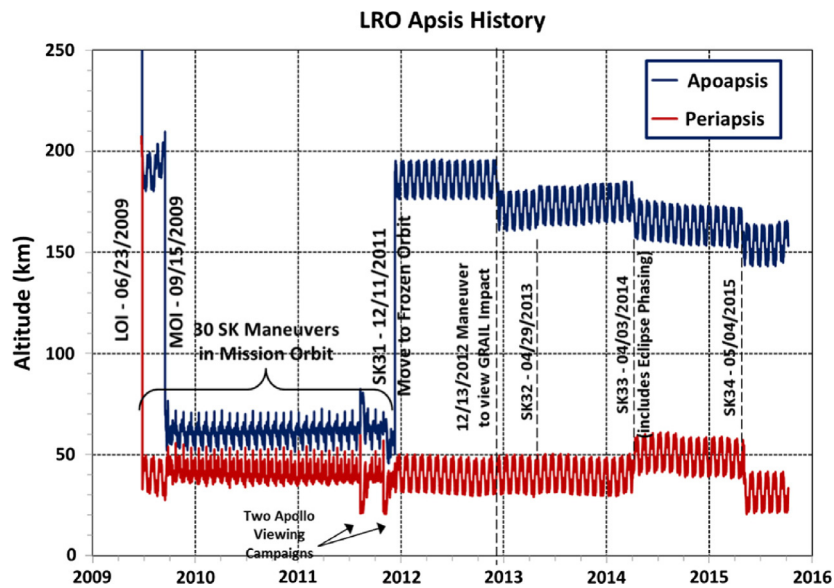


Fig. 3. Orbit history of LRO from orbit insertion in June 2009 through mid-2015. As mission objectives have evolved, the apo- and periapsis of the polar LRO orbit has been modified to maximize science return. Since December 2011 LRO has been in a “Frozen” orbit that requires minimal fuel to maintain.

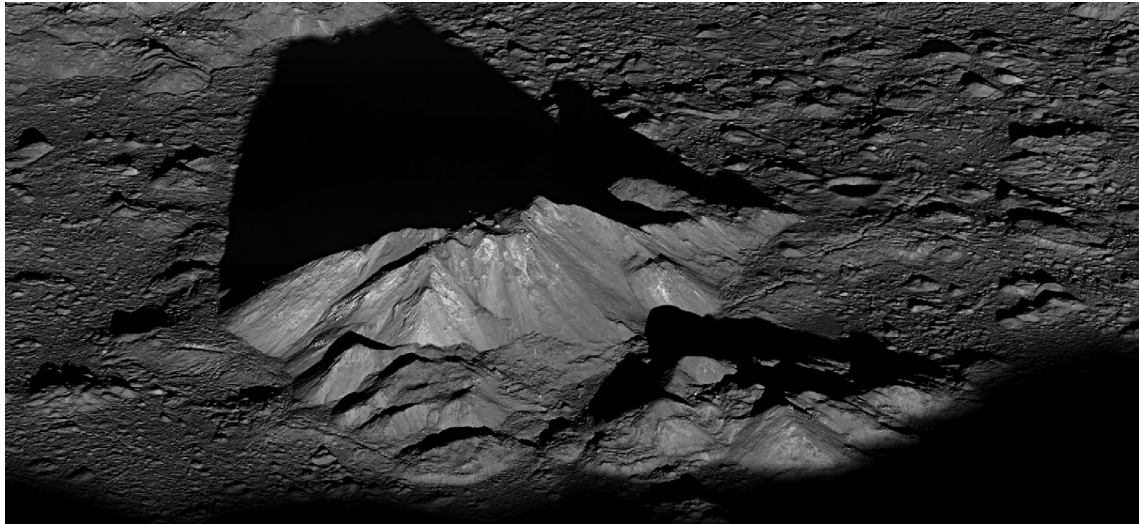


Fig. 4. Tycho crater's central peak complex, shown here, is about 15 km wide, left to right (southeast to northwest in this view). LROC NAC image M162350671 [NASA/GSFC/ASU].

would be eroded due to the Lyman- $\alpha$  background from the local interstellar medium, but calculations by Crider and Vondrak (2003) showed that micrometeorite gardening of the regolith can preserve the water beneath the surface. The neutron spectrometer onboard the Lunar Prospector spacecraft provided strong evidence of polar water based on the measured epithermal neutron flux leaking from the lunar surface, which is moderated by subsurface hydrogen. However ground based radar measurements of PSRs failed to produce evidence of rocky ice deposits of water (Campbell et al., 2006). This is in contrast to equivalent radar measurements of Mercury where strong signatures of water ice deposit were found (Chabot et al., 2014). The contrasting evidence at the Moon and Mercury remain a topic of considerable discussion that is further informed by data from LRO and the Mercury MESSENGER spacecraft.

Contemporaneously with LRO, new evidence for lunar water was changing our view of the Moon as a dry environment com-

pletely devoid of any water except possibly in the aforementioned polar regions. First the Moon Mineralogy Mapper ( $M^3$ ) instrument onboard the Chandrayaan-1 spacecraft measured the  $3.0 \mu\text{m}$  absorption band, evidence of a surface veneer of water or the hydroxyl radical (Pieters et al., 2009). This observation was confirmed when data from previous lunar flybys of both the Deep Impact/EPOXI (Sunshine et al., 2009) and Cassini (Clark, 2009) infrared instruments were examined. Even more surprising was the apparent diurnal dependence of the band depth, suggesting a lunar hydration cycle involving temperature driven transport of water through the exosphere. Meanwhile primordial water was discovered within pyroclastic glasses (Saal et al., 2008) upsetting previously established consensus that the giant impact that formed the Earth Moon system led to a Moon completely devoid of hydrogen.

Our views of the amount, distribution, and evolution of lunar volatiles are ongoing and we have come to understand that polar volatiles are controlled by an as yet unraveled interplay of time,

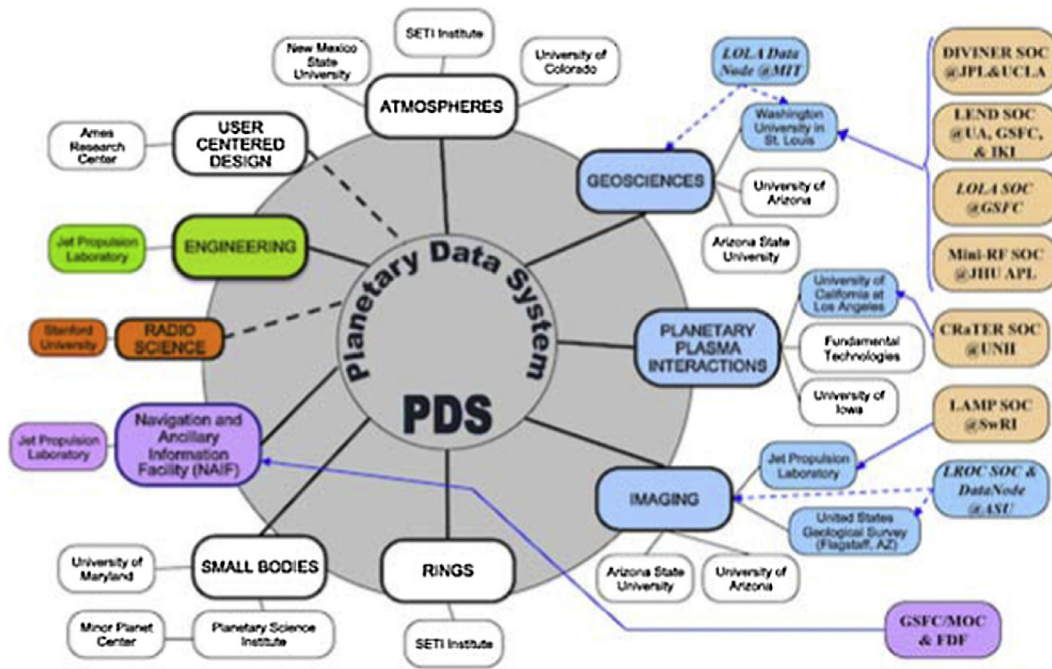


Fig. 5. Illustration of the relationship between the LRO instrument team Science Operation Centers and PDS nodes.

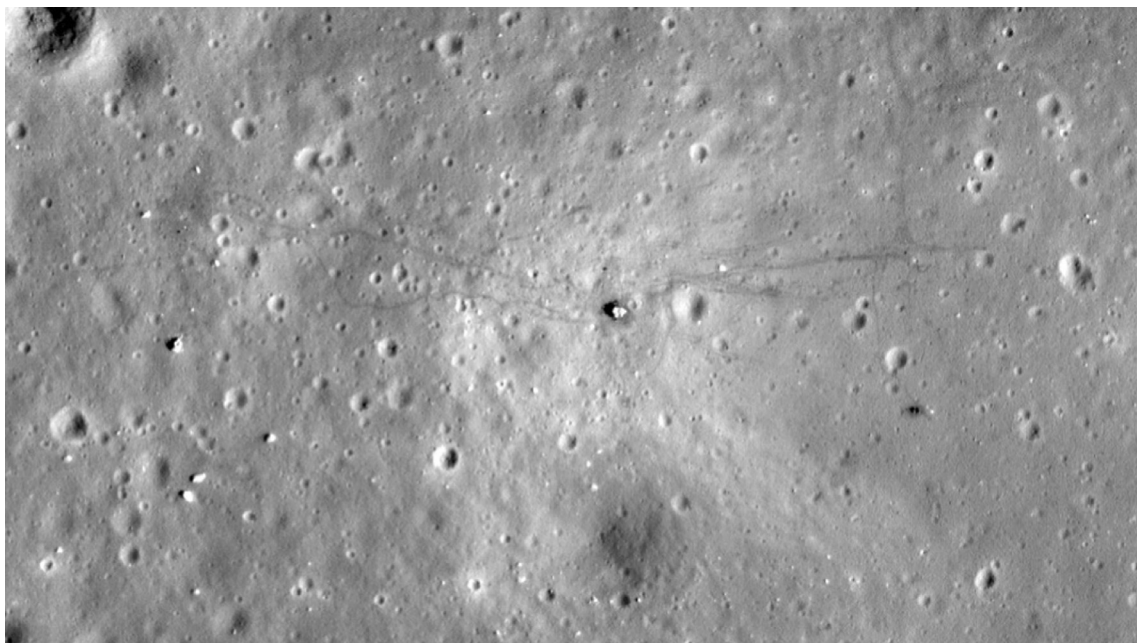


Fig. 6. LROC NAC view of the Apollo 17 landing site and its immediate surroundings. The locations of the descent stage, lunar rover, and ALSEP site are clearly visible, as are the astronaut footpaths and rover tracks. LROC image M129086118 [NASA/GSFC/ASU].

temperature, topography and the properties of the regolith. The LRO mission continues to play an important role by providing clues and constraints on these aspects of the lunar water cycle, as well as direct evidence of lunar hydrogen and water variations.

### 5.1.1. Subsurface hydrogen (water ice)

An important early result from the LRO mission used the collimated epithermal neutron detector on the LEND instrument to map epithermal neutron flux from the lunar surface with a spatial resolution of  $\sim 10$  km (Mitrofanov et al., 2010b), which showed that there are local Neutron Suppression Regions (NSRs) near the poles

that are consistent with hydrogen buried in the lunar regolith. The Lunar Prospector Neutron Spectrometer (LPNS) showed a significant reduction in the flux of epithermal neutrons in the vicinity of both lunar poles (Feldman et al., 1998, 2000), but lacked sufficient spatial resolution to determine whether hydrogen is concentrated in PSRs. Localized Neutron Suppression Regions (NSRs) mapped by LEND were found within some PSRs, such as Shoemaker and Cabeus, but they are not present in all PSRs and some NSRs were found in sunlit areas (Mitrofanov et al., 2010b, 2012; Sanin et al., 2012). Significant deposits of lunar water or hydrogen outside of PSRs may ultimately prove valuable as an exploration

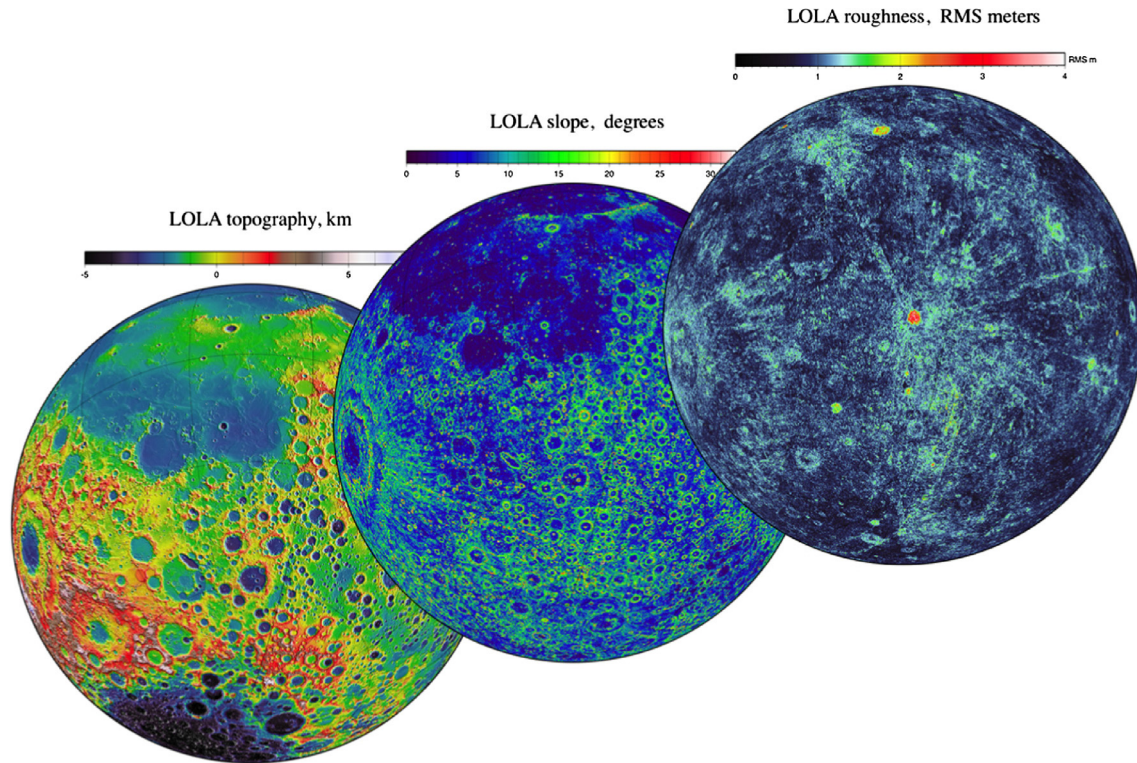


**Fig. 7.** Illustration of LOLA global map-products available on the Planetary Data System (PDS), all are centered over the crater Tycho. Included here are topography (left), derived slope (center), and derived roughness (right).

**Table 2**

List and locations of Constellation regions of interest. Each site has been imaged completely by the LROC NAC.

| Near side site       | Latitude | Longitude | Far side site                | Latitude | Longitude |
|----------------------|----------|-----------|------------------------------|----------|-----------|
| North pole           | 89.6     | 76.19     | Compton/Belkovich Th Anomaly | 61.11    | 99.45     |
| Peary Crater         | 89       | 76        | Mare Moscoviense             | 26.19    | 150.47    |
| Anaxagoras Crater    | 73.48    | -9.3      | Dante Crater                 | 26.14    | 177.7     |
| Mare Frigoris        | 59.8     | 26.1      | King Crater                  | 6.39     | 119.91    |
| Humboldtianum        | 54.54    | 77.14     | Mare Smythii                 | 2.15     | 85.33     |
| Plato Ejecta         | 53.37    | -5.21     | Hertzprung                   | 0.09     | -125.56   |
| Gruithuisen domes    | 36.03    | -40.14    | Dewar (Stratton)             | -2.08    | 166.88    |
| Lichtenberg Crater   | 31.65    | -67.23    | South Pole-Aitken Basin Rim  | -5       | -170      |
| Aristarchus 2        | 27.7     | -52.4     | Aitken Crater                | -16.76   | 173.48    |
| Rimae Prinz          | 27.41    | -41.72    | Tsiolkovsky Crater           | -19.35   | 128.51    |
| Apollo 15            | 26.08    | 3.66      | Orientele 1                  | -26.2    | -95.38    |
| Aristarchus 1        | 24.56    | -48.95    | Van De Graaff Crater         | -26.92   | 172.08    |
| Sulpicius Gallus     | 19.87    | 10.37     | Mare Ingenii                 | -35.48   | 164.42    |
| Ina (D-caldera)      | 18.65    | 5.29      | Apollo Basin                 | -37.05   | -153.72   |
| Marius Hills         | 13.58    | -55.8     | Mendel-Rydberg Cryptomare    | -51.14   | -93.07    |
| Rima Bode            | 12.9     | -3.8      | SPA Basin Interior           | -60      | -159.94   |
| Mare Crisium         | 10.68    | 58.84     | Schrödinger                  | -75.4    | 138.77    |
| Copernicus crater    | 9.85     | -20.01    | South pole                   | -89.3    | -130      |
| Reiner Gamma         | 7.53     | -58.56    |                              |          |           |
| Hortensius Domes     | 7.48     | -27.67    |                              |          |           |
| Mare Tranquillitatis | 6.93     | 22.06     |                              |          |           |
| Murchison Crater     | 4.74     | -0.42     |                              |          |           |
| Flamsteed Crater     | -2.45    | -43.22    |                              |          |           |
| Riccioli Crater      | -3.04    | -74.28    |                              |          |           |
| Apollo 16            | -9       | 16.47     |                              |          |           |
| Alphonsus Crater     | -12.56   | -2.16     |                              |          |           |
| Montes Pyrenaeus     | -15.91   | 40.81     |                              |          |           |
| Orientele 2          | -18.04   | -87.91    |                              |          |           |
| Balmer Basin         | -18.69   | 69.82     |                              |          |           |
| Bullialdus Crater    | -20.7    | -22.5     |                              |          |           |
| Tycho crater         | -42.99   | -11.2     |                              |          |           |
| Malapert Massif      | -85.99   | -2.93     |                              |          |           |

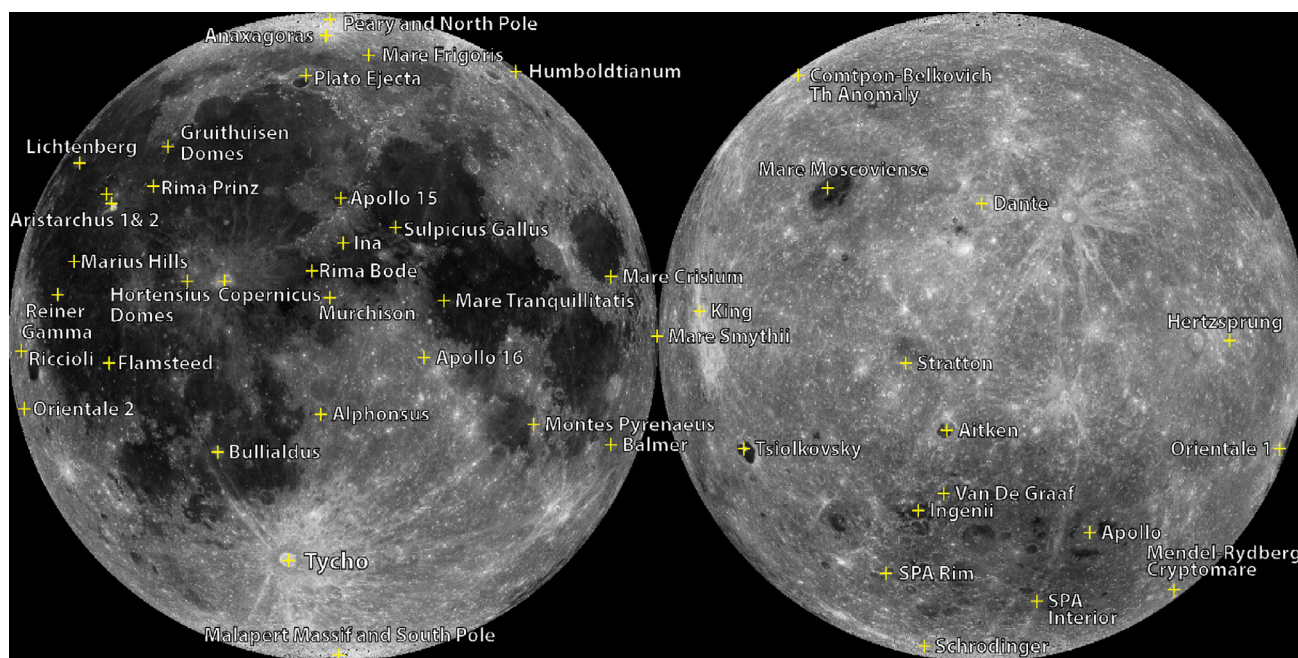


Fig. 8. Map of the location of the 50 regions of interest identified by NASA's Constellation Program. Each region represents a key location identified to characterize a lunar terrain by the LROC Narrow Angle Camera.

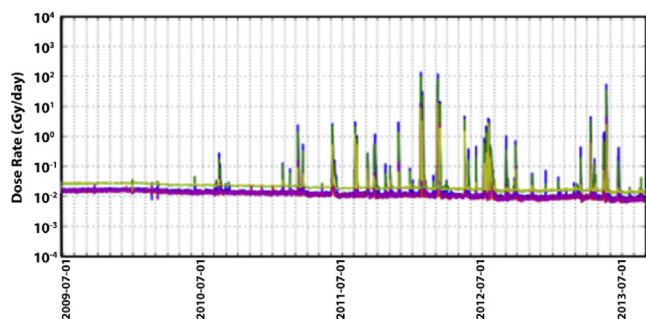


Fig. 9. Total radiation dose rates as measured by the CRA TER instrument over the first 4 years of the LRO mission.

resource. We note that the effectiveness of the LEND collimator is controversial with some researchers holding that the LEND signal is dominated by uncollimated neutrons (e.g. Teodoro et al., 2014 and references therein).

LEND data were used in selecting the impact site for LCROSS, with estimated water content in Cabeus crater of 0.5–4 wt% (Mitrofanov et al., 2010b), confirmed by direct measurements of water content by LCROSS as  $5.6 \pm 2.9$  wt% (Colaprete et al., 2010). The LEND data, in concert with LOLA, has been used to constrain processes that sequester volatiles, showing that insolation conditions may affect the distribution of hydrogen. LEND has found the concentration of hydrogen is also affected by the slope direction of the lunar surface (McClanahan et al., 2015) with pole facing slopes exhibiting greater neutron suppression, and greater hydrogen concentrations, than equator facing slopes.

LRO Mini-RF has placed additional constraints on the possibility of thick ice in PSRs. In agreement with earlier Earth-based studies, Neish et al. (2011b) showed that the Mini-RF radar signature of the Cabeus crater floor is not consistent with extensive, shallow slabs of water ice. Based on data from the Chandrayaan-1 imaging radar system, Spudis et al. (2010) suggested that ice may be present in craters near the north pole that have high Circular Polarization Ratio (CPR) values confined to the crater interior. LRO Mini-

RF data were used to further investigate this possibility (Spudis et al., 2013a).

From 2012–14 LRO Mini-RF made bistatic radar measurements with the Arecibo Observatory to acquire data on the scattering properties of the lunar surface as a function of radar beta angle (i.e., equivalent to phase angle for other remote sensing instruments) to understand the character of the opposition effect (the apparent brightening of a surface at zero phase angle), at its operating wavelength of 12.6 cm. These measurements take advantage of differences in the CPR characteristics of rough surfaces versus water ice (Hapke and Blewett, 1991; Hapke et al., 1998; Nelson et al., 2000; Piatek et al., 2004) to try and discriminate between surfaces that are rough and surfaces that harbor water ice. Data for Cabeus crater were collected by Mini-RF on several occasions and provide CPR information of the crater spanning a range of beta angles ( $\sim 0$ – $10^\circ$ ). These data (Patterson et al., 2014) indicate that floor materials of the crater show an apparent opposition effect (Fig. 10). These observations, coupled with inferences drawn from differences in the scattering response of the crater when viewed at an incidence angle of  $\sim 48^\circ$  (Neish et al., 2011b) versus an incidence angle of  $\sim 85^\circ$ , have led the Mini-RF team to suggest that water ice may be present at Cabeus crater as a relatively thin ( $\sim 10$ – $20$  cm) layer, near the surface (Patterson et al., 2014).

### 5.1.2. Surface frost

LRO LAMP exploits interplanetary Lyman- $\alpha$  sky-glow and UV starlight to illuminate the lunar surface (Gladstone et al., 2010b). LAMP is the first far ultraviolet spectrograph at the Moon since Apollo 17 in 1972. Its search for the UV spectral signature of surface water frost in PSRs identified several PSRs with spectral signatures consistent with  $\sim 1$ – $2\%$  coverage by water frost. Lyman- $\alpha$  nightside/PSR imaging also has contributed to understanding surface microphysics. The surface porosity of many PSRs is apparently  $\sim 30\%$  greater than surrounding regions as indicated by low Lyman- $\alpha$  albedo and comparison with models by Hapke (2008), suggesting that mixtures of volatiles together with variable electric fields near the terminator may create fluffy “fairy-castle” structures at the surface.

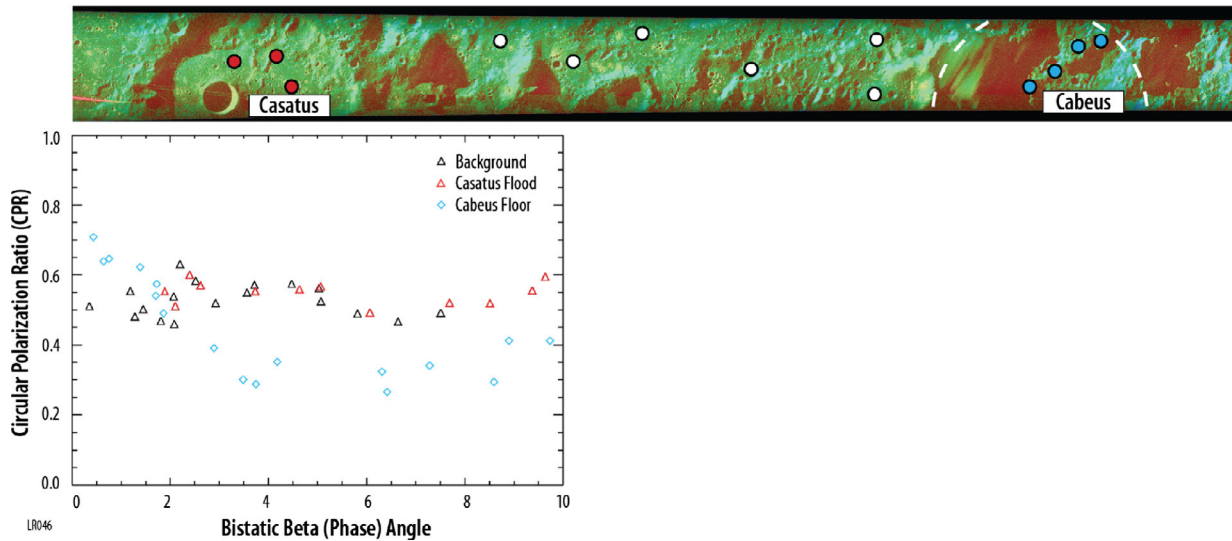


**Fig. 10.** (a) Circular polarization ratio (CPR) data acquired using Mini-RF bistatic operational mode. The crater Cabeus is outlined in dashed white. Circles represent 90 km<sup>2</sup> regions of surface where the CPR was sampled and plotted against phase angle, (b) plot of CPR vs. phase angle for Casatus crater (red), Cabeus crater (blue), and surrounding terrain (white/black), Cabeus crater shows a clear opposition effect that is distinct from surrounding terrain and nearby Casatus crater.

LRO LOLA actively senses the albedo of PSRs with its 1064 nm laser, discovering enhanced IR reflectance in Shackleton crater and slightly enhanced reflectance in a few other PSRs. Zuber et al. (2012) observed anomalous high reflectance material on the walls and floor of Shackleton crater possibly due to downslope movement or surface frost (Fig. 11). The interior walls of Shackleton are brightest, likely due to fresh material exposed as other material slides down the steep walls. The floor is brighter than the surrounding area (outside the crater), consistent with ~10% by area water frost abundance. The LOLA albedo measurements are made globally and enable the identification of other areas of transient surface change, possibly due to volatile migration.

Although our views concerning water and other volatiles on the Moon have changed, the local abundance of water at the poles as observed by LRO and other mission is by no means great, based on results to date. While evidence of surface water frost in PSRs has been developed by LRO, the amount appears to be much smaller than on Mercury. Visible images of PSRs (using highly stretched images illuminated by faint reflected light) on Mercury show areas of enhanced reflectance (Chabot et al., 2014) while images of lunar PSRs from LRO NAC show no corresponding change in reflectance, as was also the case with imagery of the interior of Shackleton crater as observed by the Kaguya spacecraft (Haruyama et al., 2008). Along with the radar data, the contrasting difference between polar craters on Mercury and the Moon remain unexplained but may be due to cometary or asteroidal impacts on Mercury (e.g., Moses et al., 1999; Paige et al., 2013) which led to a large amount of trapped volatiles in Mercury PSRs. An alternative theory is that since Mercury's spin axis is relatively stable (since capture into 3/2 spin-orbit resonance), Mercury's PSRs have been active for much longer while the Moon's spin axis has evolved more recently due to perturbations by Earth (Siegler et al., 2011, 2015).

### 5.1.3. Transient volatile migration

A surprising result from the Deep Impact lunar observation (Sunshine et al., 2009) is evidence of a lunar hydration cycle involving temperature driven transport of water through the exosphere. LRO has found evidence of diurnal variations in both LEND and LAMP data. The LAMP observations of UV reflectance from the lunar surface (Hendrix et al., 2012a, 2012b) are consistent with the Deep Impact result. However, LEND probes beneath the surface down to ~1 m, so the diurnal LEND variation (Livengood et al., 2015) is difficult to explain, but may be due to more than

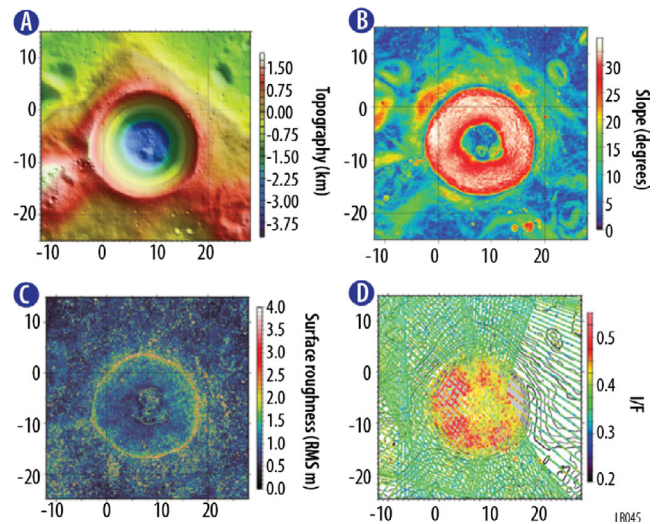


**Fig. 11.** LOLA derived topographic data (A) and derived products for Shackleton crater including (B), 10-m baseline slopes in degrees, (C) surface roughness shown as RMS residual in m, and (D) zero-phase, 1064-nm reflectance shown as I/F.

one physical process (e.g., a small temperature dependence of neutron moderation in the regolith (Little et al., 2000), temperature-driven vertical transport of hydrogen (Schorghofer and Taylor, 2007), as well as exospheric transport of water).

### 5.1.4. Physical characteristics of the lunar poles

The polar orbit of LRO results in a high density of observations of the lunar poles; LRO data is being used to extensively characterize the polar regions of the Moon. Detailed day night temperature profiles at different seasons along with thermal models by the Diviner team map out regions of stability of numerous volatiles including water (Paige et al., 2010b). High resolution LOLA topography of the polar regions, a result of LRO's polar orbit leading to a dense mesh of measurement points, are used to map PSRs with high precision and allows modeling of multiple reflections to find doubly shaded regions of small craters within PSRs. LOLA topographic models of lighting conditions are verified by the direct measurements by LROC imagery of the poles throughout the lunar

year. These measurements deepen our understanding of volatile sequestration on the Moon and by extension to other Solar System bodies with surface-bounded exospheres.

An important one-time measurement of lunar volatiles came about as a result of the LCROSS impact when the LRO orbit was adjusted to make observations of the plume arising from Cabeus crater. The LAMP observations (Gladstone et al., 2010a; Hurley et al., 2012) indicated that the impact plume had a temperature of  $\sim 1000$  K with significant quantities of  $H_2$  ( $\sim 120$  kg), CO ( $\sim 570$  kg), Mg ( $\sim 40$  kg), Ca ( $\sim 160$  kg), and Hg ( $\sim 120$  kg) released by the impact. The large amount of molecular hydrogen observed is surprising since it is not expected to be trapped thermally at PSR temperatures (Paige et al., 2010b) but its presence has implications for interpretations of neutron measurements solely on the basis of water and may be partially explained by sub-surface GCR radiation chemistry (see Section 5.5). LAMP also observed the much energetically smaller GRAIL impacts from a greater distance than for LCROSS; however, a variation in observing geometry where the GRAIL impact was observed against the darkened lunar surface enabled the detection of atomic hydrogen and mercury in the plumes (Retherford et al., 2013).

## 5.2. Lunar geologic processes

### 5.2.1. Impact history of the Moon

The lunar surface has long been used to characterize how impacts craters and basins shape the surfaces of all planetary bodies (e.g., Shoemaker, 1962). As a natural laboratory for studying the impact process, the Moon offers nearly pristine examples of the role of cratering in planetary surface evolution. Prior to the LRO dataset, the lunar surface had been imaged and measured at a range of scales, but never at the combined global and high-resolution scale, as well as the wide range of illumination angles, that have been accomplished by the LRO instruments.

### 5.2.2. Chronology of lunar impacts

Data from LRO have enabled an unprecedented perspective on the flux of objects across geologic time, from the earliest ages of lunar history to the present. Using the superposed crater density, the relative and model ages of impact craters is determined using a wider range of crater sizes than previously possible, from a few meters to 100s of km in diameter. For example, basin and crater size distributions have been shown to change over geologic time, such that older highland craters are preferentially larger than younger mare craters, suggesting shifts in the impactor population characteristics over geologic time (Head et al., 2010; Kadish et al., 2011; Kirchoff et al., 2013; Morbidelli et al., 2012). These studies are enabled by the consistent geometry, high spatial resolution, and density of coverage by the LOLA and LROC instruments.

At regional and local scales the image resolutions of the LROC WAC and NAC's are critical for detailed crater counting, which has improved the precision of absolute model ages of lunar craters. Relative-age determination using crater counts is a complex function of impactor characteristics and target properties. For example, identical impacts into loosely consolidated regolith vs. solid impact melt deposits of the same age make different sized craters owing to different physical properties of the target, resulting in different apparent age for deposits known to be the same actual age. NAC data were used to improve the use of this important method in planetary surface investigations in light of these new results. One of the key results so far is an improved age for Copernicus crater derived from crater counts on its ejecta deposits. The new age resolved the long-standing problem of Copernicus, one of the most important craters that was presumably dated using Apollo 12 samples, but failed to fit the lunar crater production function (Hiesinger et al., 2012). The age of Copernicus derived from LRO images was shown to be consistent with the age derived from the Apollo 12 samples (see Fig. 12).

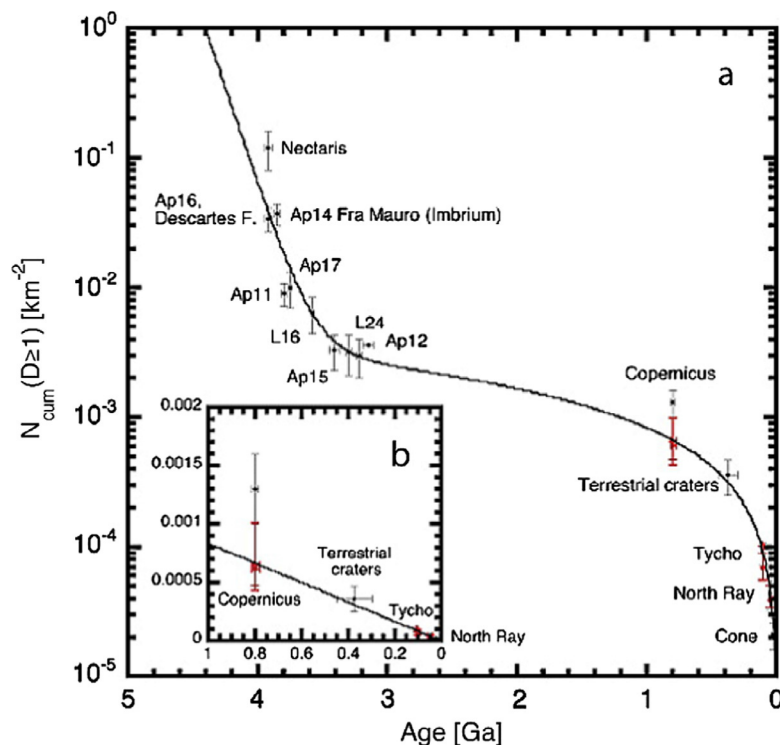


**Fig. 12.** (a) Lunar cratering chronology of Neukum and Ivanov (1994) and Neukum et al. (2001) in log linear format. Crater count analysis of LRO data shows an improved fit while LRO data (in red) for Tycho and North Ray confirm previous estimates (Hiesinger, 2012). (For interpretation of the references to colour in this figure legend, the reader is referred to the web version of this article.)

### 5.2.3. Effects of impacts on planetary surfaces

Imaging, topographic, radar, and thermal data from LRO are used to investigate the shape characteristics of craters and distribution of materials ejected by impacts with unprecedented detail and clarity. This information provides the means to understand the composition and physical characteristics of target materials and to determine lateral and vertical variability of crustal materials. The near-pristine state of many of the Moon's impact craters preserves diagnostic features such as impact melt and granular flows (Ashley et al., 2012; Bray et al., 2010; Carter et al., 2012; Denevi et al., 2012), and structures associated with crater formation such as uplifted central peak and peak-ring mountains, rim terraces, and interior and exterior deposits (Baker and Head, 2013; Baker et al., 2011, 2012; Bell et al., 2012). The identification of impact melt deposits around small craters is enabled by the globally distributed measurements by Mini-RF. Carter et al. (2012) characterized, using derived Circular Polarization Ratio maps, impact melts that in many cases are difficult to distinguish in image data. The uniform global coverage of the LOLA instrument enables detailed characterization of the surface and the structure of impact features. The well-preserved nature of the Orientale Basin has enabled a series of detailed investigations into its structure (Nahm et al., 2013), volcanic filling history (Whitten and Head, 2013), and ejecta deposits (Fassett et al., 2011). The characterization of Orientale has allowed for an improved understanding of the formation of large craters and basins such as Schrodinger (Kramer et al., 2013).

Impact crater formation and degradation processes vary according to crater size, impact angle and velocity, and as a function of target properties. Small craters formed in crystalline rock

substrates differ from those formed in thick, highland regolith deposits. LRO's high-resolution imaging, topographic, radar, and surface roughness data are all contributing to new assessments and understanding of how impact size and target characteristics affect the cratering process (e.g., Baker et al., 2011).

LRO measurements have also enabled an unprecedented view of the modification effects of cratering on the surface of the Moon. Diviner nighttime thermal observations have created a global map of surface rock abundance and soil temperatures that reveal blocky ejecta associated with fresh craters (Bandfield et al., 2011), some of which may be located antipodal to young, large craters (Bandfield et al., 2015; Williams et al., 2015). Diviner data also revealed "cold spots" surrounding geologically recent impacts around the entire lunar surface (Bandfield et al., 2014). These thermophysically distinct ejecta deposits, which may be due to proximal disruption of the regolith by surface-bound granular flow, extend 10–100 crater radii and may be common to all small craters on small bodies, yet disappear over geologic time.

Additionally, comparisons of optically immature craters on the Moon and Mercury has allowed for improved comparisons on the relative rate of space weathering and the impact flux across the inner Solar System (Fig. 13) (Braden and Robinson, 2013). The impact flux also drives rock breakdown and regolith evolution and Diviner thermophysical properties have been used to constrain this chronology (Ghent et al., 2014).

### 5.2.4. Contemporary lunar impacts

A dramatic result is the identification of LRO-era impact craters. That is, craters that formed while LRO has been in orbit. LROC has acquired high-resolution images for more than 70% of the surface,

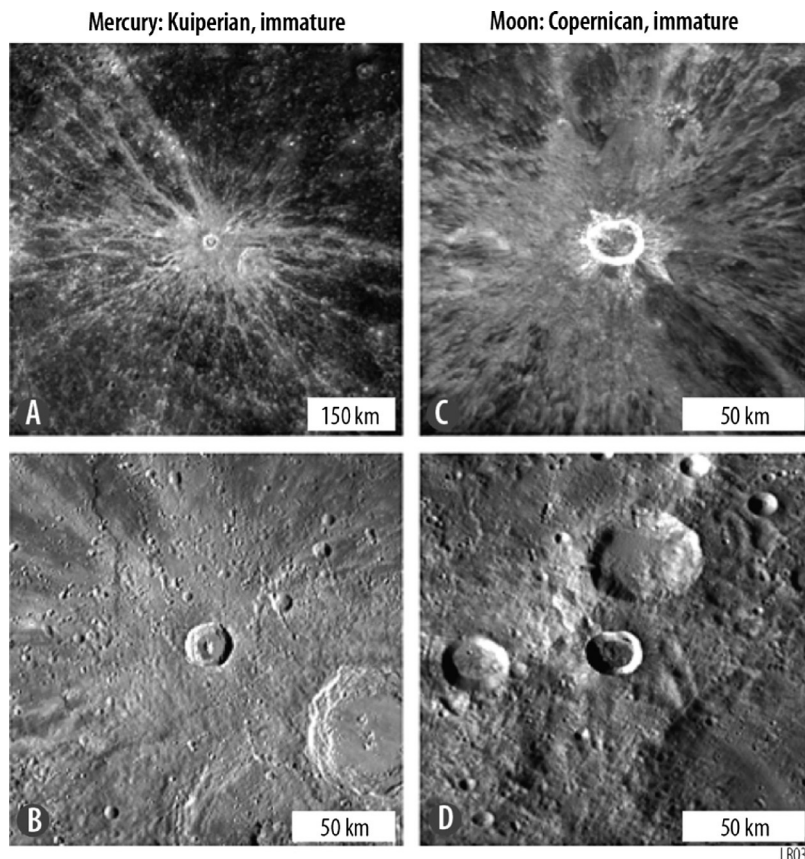


**Fig. 13.** Comparison of two bright craters from the mercurian Kuiperian and the lunar Copernican crater populations. The top two images show reflectance, and the bottom two images show morphology for the same craters Xiao Zhao (left), a Kuiperian crater, with a diameter of 24.0 km, and Giordano Bruno (right), a Copernican crater, with a diameter of 22.1 km. Figure from Braden and Robinson (2013).

with repeated coverage of targeted areas with similar lighting of approximately 3% of the surface. With repeated imaging, surface changes are identified by comparing the “before” and “after” images. As an example of this, NAC imaging of an area associated with the 17 March 2013 flash observed by the NASA Lunar Impact Monitoring Program dedicated telescope facility (Suggs et al., 2014) revealed a 18 m diameter crater (Fig. 14) and numerous small areas surface reflectance changes (Robinson et al., 2015). From the diameter and depth of the imaged crater, dynamic information such as the amount of energy released and mass of material excavated, as well as impactor mass can be estimated. In this example the impactor was estimated to be 0.28 and 1.10 m in diameter with a mass between 33 and 702 kg, depending on model assumptions. The crater thus provides “ground truth” for the Impact Monitoring Program observations and calibration of their energy estimates. The nature of the surface changes distributed around the 17 March event is a key observation in terms of understanding current impact rates and properties of the projectiles. The surface changes around the crater may have formed from low-velocity secondary impacts from the 18 m crater. The alignment of the surface changes and their geographic association with rays emanating from the March crater indicates formation as low-velocity secondaries. The NAC temporal pairs revealing the changes provide a minimum estimate of the distribution of secondary material, providing the first such direct determination at this scale.

Observations of LRO-era impacts are important not only for calibrating the lunar cratering chronology but also for calibrating it throughout the Solar System. For example, observations of recently formed craters on Mars have been used to estimate the impact flux at Mars (Daubar et al., 2013). The lunar rate serves as a reference for the other bodies; thus, the better the lunar rate is known, the better the other chronologies. Understanding the current rate is also important to constrain changes in the flux over time and as a calibration of the size-frequency distribution of small bodies wandering through the inner Solar System with sizes too small to be observed telescopically.

### 5.3. Regolith characteristics and evolution

#### 5.3.1. Photometric properties of the regolith

LRO observations of the reflectance and emission behavior of the surface over wavelengths ranging from the ultraviolet to the far-infrared provide new insight into the physical properties of the regolith (e.g., roughness, porosity). Facilitated by the local time drift of LRO’s orbit and opportunities for repeat observations under

varying illumination and viewing conditions, several instruments have collected unrivaled photometric data that provide a basis for understanding the surface properties of all Solar System objects.

Imaging coverage from the LROC WAC enabled the first spatially resolved ( $1^\circ/\text{pixel}$ ), wavelength-dependent, photometric parameter maps of the Moon. These photometric parameters result in a seamless seven-color mosaic and new insights into the controls on photometry on airless bodies (Sato et al., 2014) (Fig. 15). The WAC observations allow variations in photometric parameters to be understood at high spatial scales ( $0.5^\circ/\text{pixel}$ ) and permit, for the first time for a planetary body, global color studies. Additionally, special observation campaigns have been undertaken to increase the photometric coverage near the poles, where normal observations result in limited phase angle coverage. A series of pitch campaigns when the solar beta angle is favorable has pushed the photometric coverage of the WAC data to higher latitudes ( $\sim\pm 70^\circ$ ).

#### 5.3.2. Thermophysical properties of the lunar regolith

The lunar regolith is vertically and laterally heterogeneous, and its detailed structure reveals important information about its formation and evolution. Diviner data has shown that the uppermost 2–15 cm of regolith has extremely low density and thermal conductivity, and that the most likely density structure in the upper meter varies exponentially with depth (Vasavada et al., 2012; Hayne et al., 2013). Nighttime regolith temperatures (Bandfield et al., 2011) are strongly influenced by small rocks (<50 cm) on the surface, and larger rocks buried under several cm of the regolith. Comparison of Diviner temperatures to thermal models constrain the regolith thermal inertia in any given location where sufficient data are available (Hayne et al., 2013) which in turn provides information on the regolith’s physical properties, with intriguing variations associated with specific geologic units (Fig. 16).

Preliminary Diviner emission phase function (EPF) measurements (acquired near 11:00 local time near  $52^\circ\text{S}$ ) revealed that surface brightness temperatures, derived for a single surface point observed at different angles, varies by more than 60 K (Bandfield et al., 2011). The temperature dependence is controlled by the degree of surface roughness, generally at the smallest scale that maintains thermal isolation (few mm for highly insulating regolith), illumination, and viewing geometry. These EPF observations characterize surface roughness at mm to cm scales, providing details on regolith formation and development. In addition, initial EPF observations show a general trend of decreasing emitted radiance with increasing emission angle, regardless of viewing azimuth, latitude, or local time.

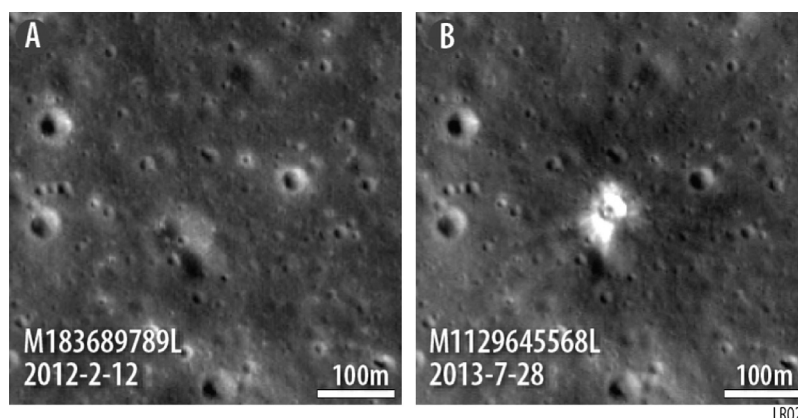


**Fig. 14.** Temporal pair of LROC NAC images showing the 18-m diameter impact crater that was observed from Earth on March 17, 2013. LRO era impact craters provide a unique laboratory for studying hypervelocity impacts and to determine the current flux of meteoroids.

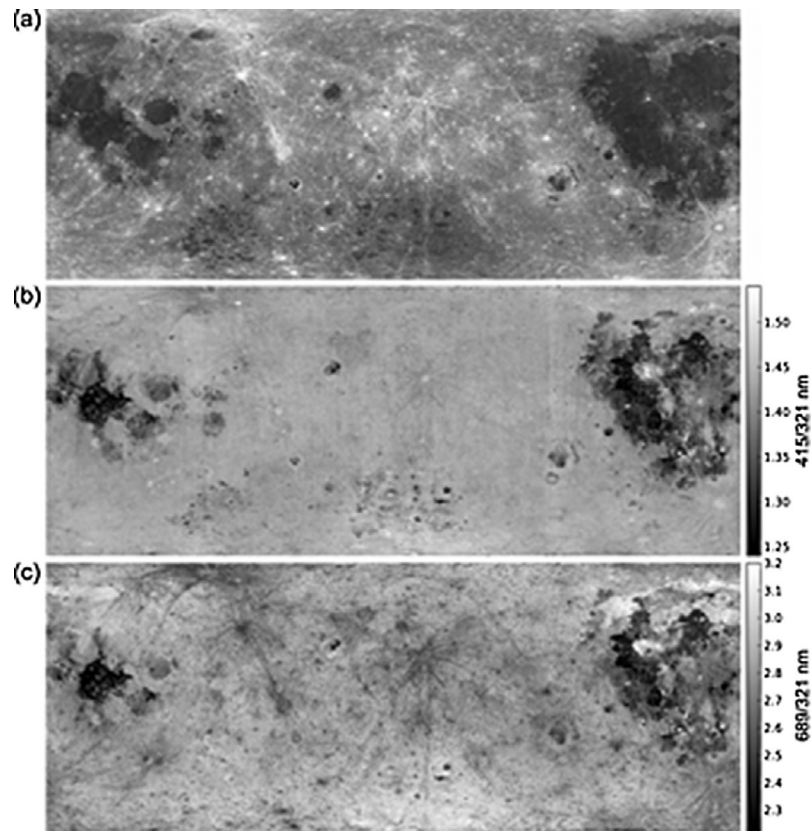


**Fig. 15.** LROC WAC derived mosaics of the lunar surface showing the quality of the camera and its photometric calibration. (a) Mosaic (median of  $n/F$  from 21 months WAC data) in RGB color composite (red: 689 nm, green: 415 nm, blue: 321 nm), (b) ratio map of 415/321 nm bands, (c) ratio map of 689/321 nm bands, for 70°S to 70°N, 0–360°E in equirectangular map projection. (For interpretation of the references to colour in this figure legend, the reader is referred to the web version of this article.)

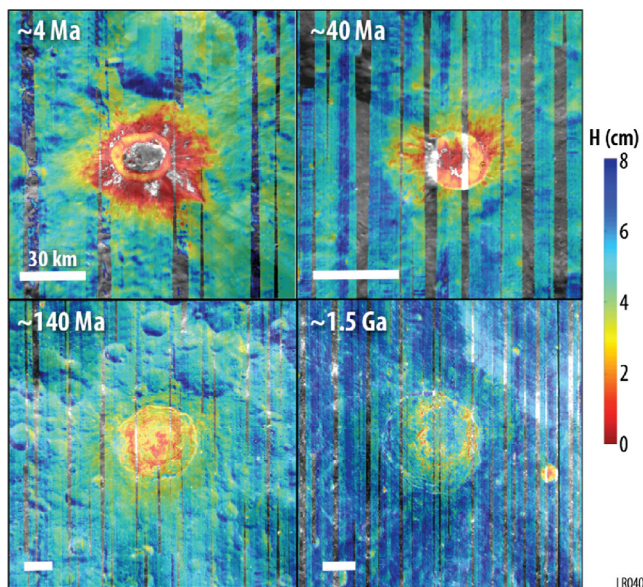


**Fig. 16.** Diviner-derived parameterization of the regolith illustrating the formation and evolution of regolith surrounding lunar impact craters. The parameter  $H$ , which is the thermal scale height of density variation in the upper meter of regolith (Hayne et al., 2013). The scale height increases with age as the regolith matures.

While Diviner's diurnal measurements generally probe the thermophysical properties of the upper meter of regolith (Vasavada et al., 2012), the rapid cooling of the lunar surface during a lunar eclipse offers a unique opportunity to remotely probe the upper few millimeters of the surface (see Operations section above). Un-

expectedly large eclipse surface cooling observed by Diviner during an eclipse (Greenhagen et al., 2015; Paige et al., 2015) suggests the widespread presence of a highly insulating layer with approximately half the thermal inertia previously modeled. Warmer eclipse temperatures near some fresh impact craters indicate the presence of exposed rocks, free of dust >1 mm thick, which could constrain the rate of dust accumulation on the lunar surface during totality. These measurements dramatically improve understanding of near-surface regolith properties and their variations among geologic features and terrain types.

### 5.3.3. Lunar swirls

Magnetically, the Moon is characterized by weak crustal fields that may be remnant of an extinct dynamo or the result of basin-forming impacts, the latter hypothesis is indicated by the antipodal location of areas of anomalously high magnetic fields. At many of the high field regions are imprinted on the surface numerous enigmatic albedo features of alternating light and dark lanes in sinuous or swirl like patterns (see Fig. 17). These lunar swirls represent an expression of the anomalous magnetic fields where neither the origin of the fields nor the swirls is fully understood. Theories on the origin of lunar swirls include the control of space weathering through shielding of the solar wind via the formation of mini-magnetospheres above the fields. Other prominent ideas invoke cometary collisions at or near the crustal anomalies (Bruck Syal and Schultz, 2015), or electrostatic transport of fine grain dust which sort dark magnetized dust particles from lighter unmagnetized particles (Garrick-Bethell et al., 2011). While LRO does not include a magnetometer in its instrument suite, instead the LRO data analysis relies on identification of magnetic field enhancement maps made by both the Lunar Prospector and Kaguya spacecraft.

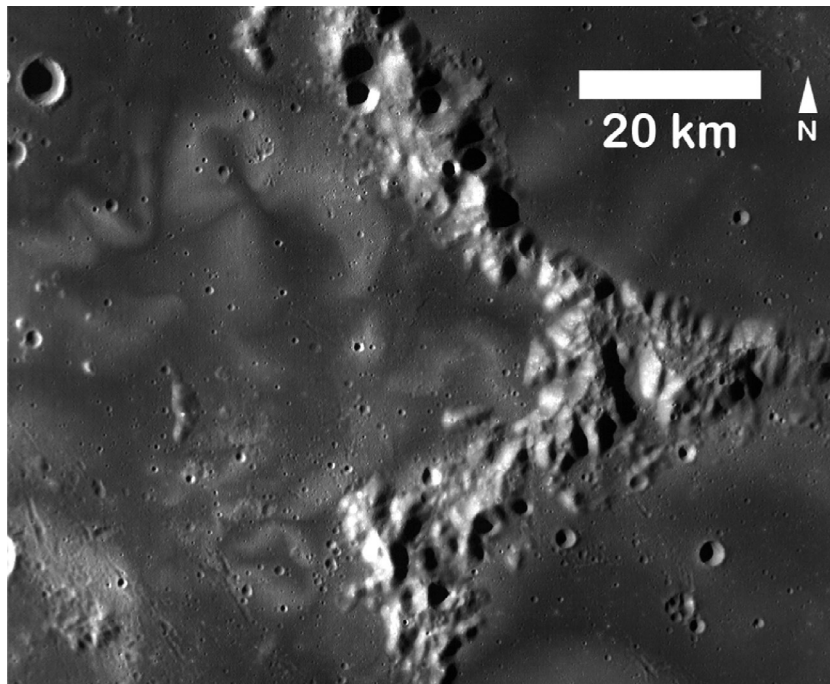


**Fig. 17.** LROC WAC image of part of Mare Ingenii illustrating the extraordinary patterns of lunar swirls. Data from multiple instruments are used to interpret the origin of swirls (Glotch et al., 2015).

Measurements by Mini-RF, Diviner, LROC, and LAMP have provided important insight into the state of the swirls and clues to understanding their formation. Swirls do not appear in the radar images from the Mini-RF instrument which is an indication that the swirls are surface manifestation and do not extend to the depth of few radar wavelengths (Neish et al., 2011a). Thermal infrared data from the Diviner instrument (Glotch et al., 2015) display an anomaly in the position of the silicate Christiansen Feature consistent with reduced space weathering. These data also show that swirl regions are not thermophysically anomalous, that is the regolith properties in swirls are indistinct from their surroundings (apart from albedo), yet are distinct in terms of degree of space weathering. This result strongly constrains their formation mechanism and supports the shielding from the solar wind by a mini-magnetosphere mechanism of swirl formation. Observations in the UV by the WAC (Denevi et al., 2014) and the LAMP far-UV (Hendrix et al., 2015) provide additional evidence on the state of space weathering in the swirls, supportive of the mini-magnetosphere hypothesis although questions still remain and more research is needed.

#### 5.4. Clues to interior processes based on surface observations

##### 5.4.1. Young, small-scale contractional and extensional landforms

Tectonic landforms are a direct expression of the evolution of stresses in a planetary crust. LRO has characterized, in unprecedented detail, small- and large-scale tectonic landforms across the Moon. LROC images reveal a population of previously undetected small-scale contractional and extensional structures on the nearside and in the farside highlands (Banks et al., 2012; Watters et al., 2010, 2012). An example is shown in Fig. 18. Detailed analysis of lobate scarps using LROC WAC and NAC images and topographic data obtained from LOLA and LROC stereo imaging, show the Moon is in a general state of global contraction due to interior cooling. The scarps found on the Moon can be compared to analogous scarps on Mercury and Mars that can have over a kilometer of relief. In contrast, known lunar lobate scarps generally have a maximum relief of <100 m and proportionately smaller lengths.

Previously undetected small-scale extensional troughs or graben are also revealed in NAC images. These graben are found both

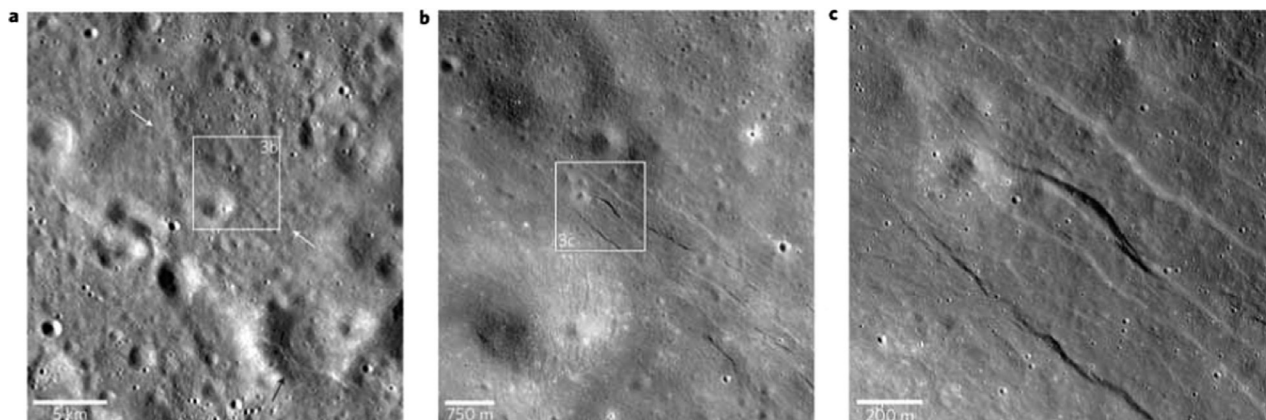


**Fig. 18.** LROC NAC images, zooming in on graben located northeast of the Virtanen Crater (Watters et al., 2012). The NAC images of lunar graben and thrust faults illustrate the global (Fig. 19), fine scale, and recent, modification of the lunar crust. LROC NAC frame M136362376LR.

in nearside mare and in the farside highlands and, like the lobate scarps, crosscut small-diameter impact craters. With depths as shallow as 1 m, these apparently pristine graben are estimated to be <50 Ma old (Watters et al., 2012). The small-scale graben indicate that extensional stresses locally exceeded global compressional background stresses from radial contraction that formed the population of young lobate scarps. The wide distribution (Fig. 19) of young lobate scarps and small-scale graben is an indicator of the geologically recent stress state of the lunar crust and thus has implications for models for the Moon's origin and thermal evolution.

#### 5.4.2. Tidal response of the lunar interior

The long time series of LOLA altimetric measurements have been used primarily to construct topographic maps. However, the thousands of intersecting ground tracks can be leveraged to detect minute time-variable changes at the cm scale in surface height due to tidal deformation by the Earth and Sun. Nearly half a million 'crossovers' were analyzed to yield a refined estimate of the tidal Love number  $h_2$ , which describes the amplitude of the tidal response, of  $0.0371 \pm 0.0033$ , independent of an interior structure model (Fig. 20). This is more precise but consistent with recent estimates derived from Lunar Laser Ranging (Williams, 2008; Williams et al., 2013), and provide better constraints on interior structure models because the LOLA measurements are indicative of a global process, rather than solely limited to the nearside e.g. Khan and Mosegaard (2005).

#### 5.4.3. New insights into lunar volcanism

The surface expression of volcanic features offers insights into internal processes that generate magmas. The wide range of LRO datasets offer distinct views into the full complement of volcanic features and their eruption histories. The global high-quality datasets have enabled a wide range of studies of lunar volcanism, from the identification of small-scale pyroclastic deposits (Gustafson et al., 2012) to determining a stratigraphic sequence for the timing of volcanic episodes (Whitten and Head, 2013). Here some of the significant findings are highlighted.

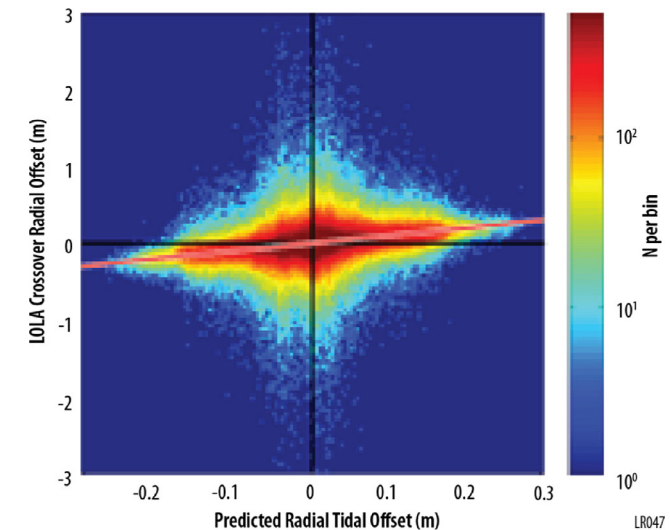


Fig. 20. LOLA data shows, for the first time from lunar orbit, the magnitude of the lunar tide. Two-dimensional histogram of the measured crossover radial offset against the predictions from a simple degree-2 tidal deformation model. The obvious trend is consistent with the *a priori* Love number  $h_2$  (Mazarico et al., 2014).

#### 5.4.4. Basaltic shields and cones

Basic aspects of mare volcanism were understood during the Apollo era, but significant questions about duration, eruption mechanics, and emplacement of mare basalts remain. The relationship between mare flood basalts, basaltic shields scattered throughout the maria, and basaltic cones is poorly understood (Lawrence et al., 2013; Stopar et al., 2014). There are numerous poorly-investigated volcanic end-members where LRO data has enabled new understandings. Previous efforts to classify basaltic shields used limited spacecraft and telescopic datasets e.g. (Head and Gifford, 1980; Wöhler et al., 2007). Repeat WAC observations under various illumination geometries and NAC imagery have enabled the identification of new candidate small shields as well as newly-identified basaltic cones (Lawrence et al., 2013; Spudis et al., 2013b). With such improved characterization of basaltic volcanism, LRO is creating an unprecedented and comprehensive

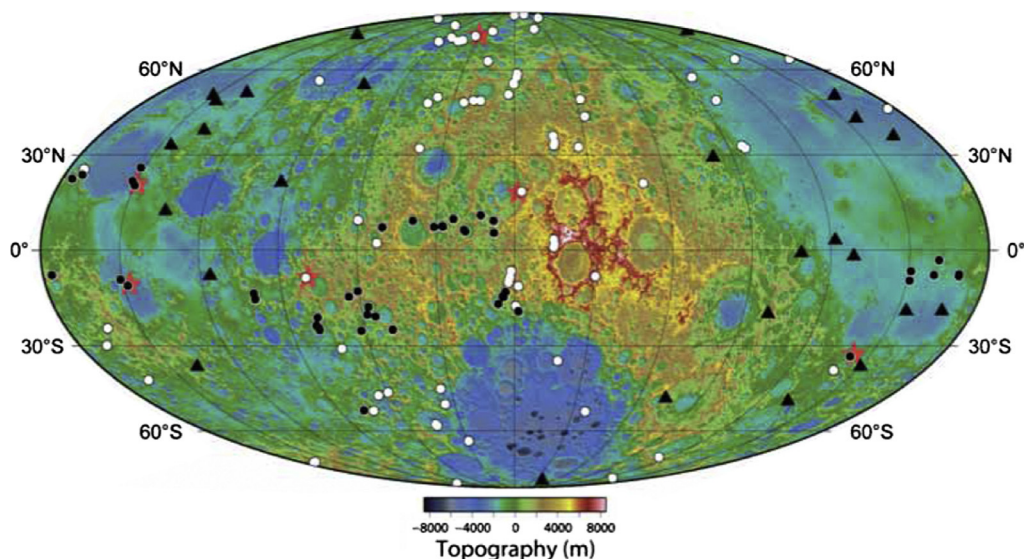


Fig. 19. Lunar-wide map illustrating the distribution of tectonic features as identified by LROC NAC images (after Watters et al., 2012). The global distribution of graben and thrust faults as identified by LROC sheds new light on the processes that drive lunar tectonism (Watters et al., 2015). In this figure the dots represent the location of lobate scarps with black and white representing known and newly discovered scarps. Triangles are the locations of shallow moonquakes identified from Apollo seismic data.

inventory of shields and cones and to identify source vents, estimate lava rheological properties, and examine regional geologic trends.

#### 5.4.5. Copernican-era volcanism

Irregular Mare Patches (IMPs) (Braden et al., 2014), such as Ina (El-Baz, 1973; Whitaker, 1972), appear to be geologically young ( $\ll 1$  Ga) volcanic feature (Fig. 21). NAC images revealed over 70 morphologically similar features previously unrecognized. Understanding these potentially very young ( $< 500$  Ma) features is critical for understanding the thermal and magmatic evolution of the lunar interior, as the presence of these features suggest that portions of the lunar interior remained warm enough for volcanism to occur for a much longer period of time than previously thought.

#### 5.4.6. Silicic volcanic complexes

LRO observations have provided the first direct evidence of large silicic rock bodies exposed at the lunar surface (Glotch et al., 2010). High-resolution imaging and topographic data from LROC and LOLA provide evidence that specific domes are volcanic, as well as the data needed to characterize compositions, morphologies, slopes, flow features, volumes, and, in some cases, associated collapse pits or calderas (collapsed terrain in the center of a volcano) and the following sites have been verified as being silicic, Hansteen Alpha, Gruithuisen domes, Mairan domes, and the Compton–Belkovich volcanic complex, (Glotch et al., 2010, 2011; Jolliff et al., 2011). The identification of the Compton–Belkovich volcanic complex, which had been recognized in Lunar Prospector data as being enhanced in thorium (Lawrence et al., 2003), located on the lunar farside and far from the main thorium enhancement on the nearside (the PKT, Jolliff et al., 2000). Subsequent analysis of the Compton–Belkovich using Mini-RF and Moon Mineralogy Mapper data (Bhattacharya et al., 2013; Petro et al., 2013) have shown an enhancement of hydration associated with the complex, and a suggestion that the complex was formed, in part, as a result of pyroclastic eruptions (Wilson et al., 2015b).

#### 5.4.7. Lunar pits and sublunarean voids

Although a lunar pit was first identified in Kaguya Terrain Camera images (Haruyama et al., 2009), LROC observations led to the discovery of 5 more mare pits and surprisingly, over 200 pits in Copernican aged impact melt deposits. Lunar pits or sublunarean voids have been identified in LROC NAC images in both volcanic and impact melts (Robinson et al., 2012; Wagner and Robinson,

2014). The distribution of such pits offer the views of both the near-pristine layering of volcanic flows as well as how magma may have flowed during the emplacement of basalts. Pits in impact-melt deposits serve to illustrate the mobility of melt-rock during the modification stage of crater formation. These pits are extremely interesting candidates for future exploration as they may offer protection from hazardous radiation and unique perspectives on the volcanic history of the Moon.

#### 5.4.8. Remote measurements of lunar heat flow

Diviner's temperature measurements within the coldest polar shadows (as low 20 K) may be able to constrain geothermal heat flux of the Moon (Paige et al., 2010b; Siegler et al., 2012, 2013). The temperatures inside several craters ( $> 5$  km in diameter) at each pole have been found to dip below 25 K each year. At the coldest points of the year, heat from below can exceed heat from reflected sunlight and reradiated heat, allowing Diviner to constrain the heat flux from the lunar interior.

The heat flux can be equated to geothermal heat production, which is used to constrain the radiogenic composition and thermal evolution of the lunar interior. Current estimates (Siegler and Smrekar, 2014) place surface heat flux from the interior ( $\sim 10$ – $15$  mW m $^{-2}$ ), generally smaller than the Apollo measured heat flow values, which are likely biased by crustal radiogenic materials and geometric focusing by the lunar mare. In that sense, the Diviner measurements near the poles may be more of a direct measurement of the heat production from the lunar mantle. The polar locations of the Diviner measurements are far from these radiogenic provinces (Jolliff et al., 2000), but can be affected by heat flowing laterally from areas with warmer average surface temperatures (Lachenbruch, 1968).

Fig. 22 illustrates the measurement approach (e.g., Aye et al., 2014), showing surface heat fluxes based on Diviner average temperatures (which represent temperatures below the yearly skin depth) using GRAIL estimated crustal density profiles. For an assumed mantle heat flux of 10 mW m $^{-2}$  we see  $> 2\times$  variations in effective geothermal heat flux at the surface. The Diviner analysis benefits from the incorporation of higher-resolution data products from GRAIL, such as precise models of crustal thickness and density (Besserer et al., 2014) that should lower the errors due to crustal density.

### 5.5. The Moon's interaction with the space environment

The Moon does not have a significant atmosphere, which is the most common condition for rocky bodies in the solar including Mercury, asteroids, comets (when sufficiently distant from the Sun), and most of the moons of the other planets in the Solar System. However, the Moon does have a surface bounded exosphere made up of particles sputtered from the surface, with possibly a contribution of gasses leaked from the Moon's interior, as well as elements delivered to the Moon by the solar wind and meteoric impacts. These impacts along with the solar wind alter the lunar surface, effectively aging it. The Moon is also altered by cosmic rays that reach deeper into the surface than solar energetic particles and micrometeoritic impacts. Thus a study of the Moon's interaction with its external environment is a study of the surface of the Moon and the processes that change it over time. This is accomplished on LRO through the LAMP instrument, which directly observes components of the exosphere, while the CRaTER and LEND instruments provide information on the lunar radiation environment.

#### 5.5.1. Global exosphere morphology

LAMP obtained the first detection of the lunar helium and molecular hydrogen using remote sensing (Stern et al., 2012, 2013),

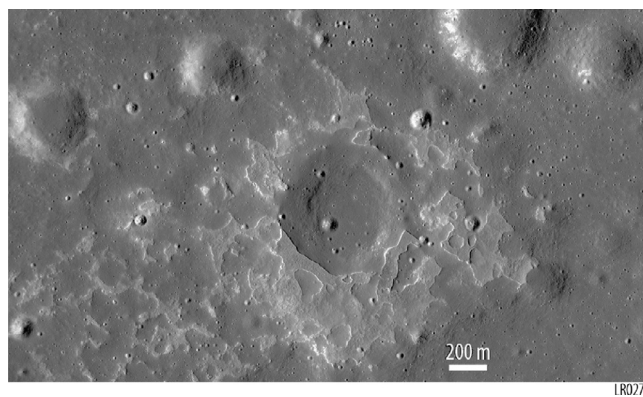


**Fig. 21.** LRO NAC view of a Irregular Mare Patch (IMP), believed to have formed within the last 100 myr. The feature called Maskelyne is one of many newly discovered young volcanic deposits on the Moon. Analysis of LROC NAC data indicate that these areas are remnants of small basaltic eruptions that occurred much later than the commonly accepted end of lunar volcanism, 1–1.5 byr ago. M1123370138R.

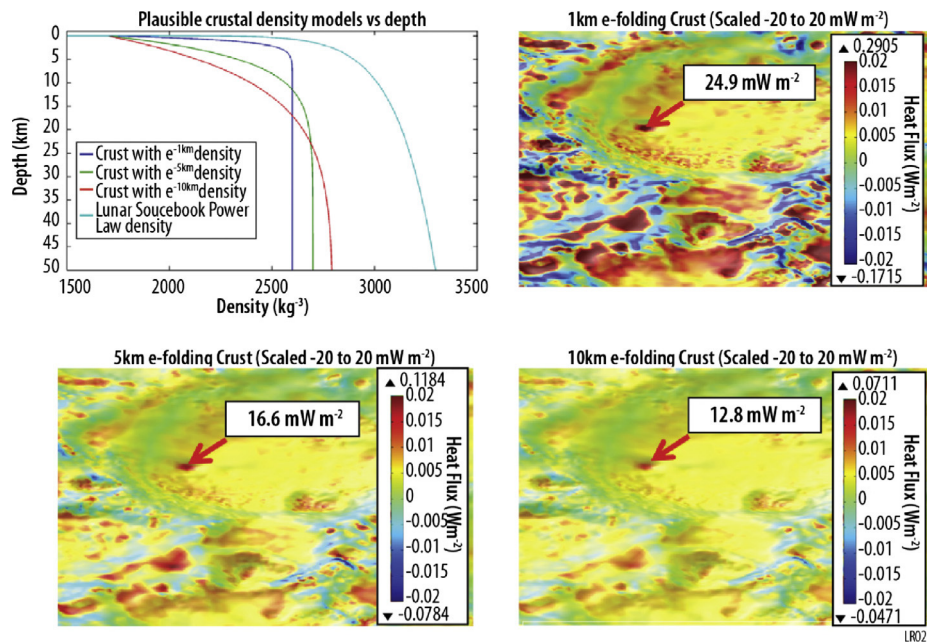


**Fig. 22.** Diviner-derived modeled surface heat flux assuming various crustal density profiles. Areas in double-permanent shadow near the poles have low measured surface temperatures and are targeted by Diviner in order to constrain heat-flux in areas far from the Procellarum-KREEP Terrain.

which was the first detection since the Apollo LACE experiment discovered helium *in situ* (Hoffman et al., 1973). Helium is formed primarily through delivery, implantation, and re-release of solar wind  $\alpha$ -particles, with perhaps 10% also formed by radiogenic decay of Th and U (Hodges et al., 1973) (Hurley et al., this volume; Grava et al., this volume). Helium is a significantly stronger signal than  $H_2$  in the LAMP instrument due to higher densities at the Moon and larger oscillator strengths of the measured fluorescence lines, enabling more detailed mapping of the He distribution. The helium distribution in the exosphere is controlled by thermal accommodation and hence surface temperature distribution, resulting in higher abundances on the nightside and the poles. Feldman et al. (2012) reported LAMP helium density variations correlated with solar wind alpha-particle density and Earth magnetotail crossings, which better constrain the timescale for the thermal accommodation process. New constraints on many other lunar atmospheric species were also obtained with LAMP (Cook et al., 2013). These studies suggest that the exosphere is controlled by surface sequestration and solar wind particle flux in ways that are complex and poorly understood until now. Joint observations searching for Ar in the exosphere by the polar orbiting LRO spacecraft, jointly with the equatorial orbiting LADEE spacecraft, now enables more detailed studies of the time and spatial variance of the exosphere.

LAMP probed the composition of impact plumes from three different satellite impacts (Gladstone et al., 2010a; Retherford et al., 2013). Dedicated LAMP searches for horizon glow, i.e., forward scattered sunlight from exospheric dust elevated to  $>1$  km, strongly constrain the possible densities and formation mechanisms for these postulated particles through model comparisons (Feldman et al., 2014).

#### 5.5.2. Interactions with cosmic rays and solar energetic particles during the solar cycle

LRO CRaTER observations provide a direct, quantitative measurement of the radiation near the Moon, which constantly bombards and interacts with the lunar regolith. Data taken during the recent solar minimum, which resulted in the largest galactic cosmic ray (GCR) intensities ever observed during the space age, pro-

vide a historical context for estimating integrated dose to lunar surface material over the lifetime of the Moon. Schwadron et al. (2011) have shown that the cumulative effect of GCR dose would likely substantially modify near-surface properties of the lunar regolith, with particularly important implications for evolution of lunar ice and other volatiles, especially in permanently shadowed regions.

The five-year baseline of GCR measurements by CRaTER occurred during an extremely unique period of solar activity. The relatively low solar maximum enables an unprecedented view of the GCR flux and its interactions with the lunar surface (Case et al., 2013; Looper et al., 2013; Schwadron et al., 2013). There are strong indications, particularly in cosmic ray data and solar magnetic field data that the Sun was behaving quite differently in this solar minimum than it has previously throughout the space age (Fig. 23). These changes have implications for our understanding of the lunar regolith, its radiation history and subsurface chemical changes across the lunar surface.

CRaTER has measured a small but significant flux of energetic particles, primarily hydrogen spallation products which are referred to as the lunar proton albedo. Initial studies by Wilson et al. (2012) indicated no regional differences in the measurements but as statistics continue to build the CRaTER team has identified (Wilson et al., 2015a) differences in highland vs. mare regions which is likely the result of compositional variation in the regolith.

Solar energetic particles (SEPs) and GCRs bombard and deposit electrical charge into the regolith, leading to substantial subsurface electric fields and possible dielectric breakdown during larger SEP events (Jordan et al., 2012). In addition, GCR and SEP bombardment breaks down molecules in the regolith, thereby affecting the chemistry in the Moon's polar regions, particularly in PSRs (Jordan et al., 2013; Schwadron et al., 2012). This makes these regions a prime target for new CRaTER observations, since CRaTER measures GCRs and SEPs that penetrate the regolith down to 10s of cm (Goswami and Lal, 1977; Pepin et al., 1974). Direct measurements of the lunar poles by CRaTER, along with several other instruments, have increased our understanding of processes affecting PSRs. Detecting  $H_2$  in the LCROSS Centaur impact plume was unexpected (Gladstone et al., 2010a; Hurley et al., 2012) but recent studies

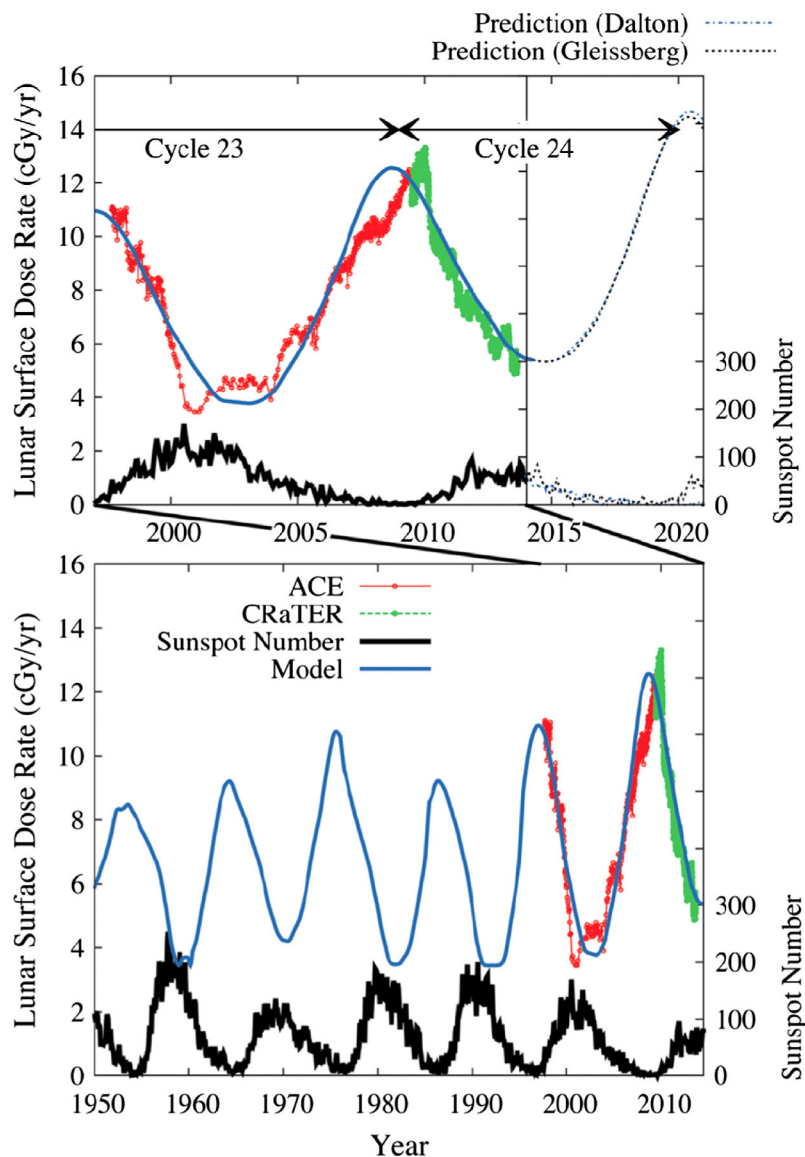


Fig. 23. Plot of historical sunspot number (right axes) and modeled and measured (ACE and CRaTER) lunar surface radiation dose (left axes).

using CRaTER data show that GCRs and SEPs can dissociate PSR H<sub>2</sub>O ice and create secondary products including H<sub>2</sub> (Jordan et al., 2013; Schwadron et al., 2012).

## 6. Support of future landed missions

The previous section describes the exciting new planetary science that has been accomplished by LRO. In addition, LRO also provides valuable measurements in support of other lunar missions, by both global mapping and by targeting of specific sites for future lunar missions. LRO can also serve as a data communications relay for landed systems that do not have line of sight access to Earth.

### 6.1. Site selection for future landers

LRO data, especially NAC high-resolution images and NAC-derived high-resolution geometric stereo digital terrain models (DTMs), are likely to be the highest spatial resolution terrain analysis products available for many years, so it is important to collect the data now that will support landed missions for the foreseeable

future. These data, when combined with roughness measurements from LOLA, Diviner, and Mini-RF, provide ample data to support landing site analysis. Additionally, data from several of the instruments, such as Mini-RF, LOLA, and LAMP, provide important constraints on the properties of areas in permanent shadow, enabling future exploration in those key regions.

Future potential landing sites on the Moon include sites for NASA's New Frontiers candidate missions (e.g., South Pole-Aitken Basin sample return or the Lunar Geophysical Network), Discovery missions, polar resource missions such as HEOMD's Resource Prospector, and international missions such as ISRO's Chandrayaan-2, for which high resolution DTMs have already been produced at the request of NASA HQ. Because acquisition of images suitable for geometric stereo solutions is constrained by illumination requirements and the need to slew the spacecraft, coverage of key science regions of interest other than the 50 Constellation ROIs remains sparse. Additionally, Diviner compositional and thermophysical datasets are unique and unprecedented views into the geology and geomorphology of potential landing sites and Diviner temperature data can provide key inputs for engineers planning to survive lunar night and/or permanent shadow.

## 6.2. Possible communications relay

In addition to data products used by future missions, LRO is capable of serving as a data relay for assets on the surface of the Moon. This is particularly valuable for missions without direct view of the Earth on the lunar farside and in polar craters.

## 7. Conclusions

The LRO mission is taking place during a period of renewed interest in the Moon with numerous missions by space faring nations and with many more planned. LRO is poised to support future missions with continued global mapping and with concentrated data acquisition over potential landing sites including the creation of high resolution stereo mosaics. Additionally, the LRO spacecraft is capable of acting as a communications relay for sites that lack line-of-sight access to Earth.

LRO has advanced our understanding of the history of the Moon and Solar System while elucidating processes that have taken place in the recent geological past, or are continuing in the present. With many of our basic assumptions about the Moon having been overturned, new questions have emerged that can be answered with additional study by LRO and future orbital and landed missions. LRO will provide unique observations that address questions outlined by the Decadal Survey, NASA's Science Mission Directorate objectives, as well as measurements critical for human spaceflight beyond low Earth orbit. Going forward in its extended Science Mission, LRO will continue investigations of volatile emplacement and transport, its current geological stress state and the effect of tidal forces acting on it, its thermal history, the regolith and its formation through the interaction of the external environment, including current impacts and the radiation environment.

## Acknowledgments

LRO accomplishments are the result of the LRO Science Team that developed the LRO instruments and analyze the observations, as well as the LRO Project at Goddard Space Flight Center that developed and operate the LRO spacecraft. Special thanks are due to the Principal Investigators for their leadership of their instrument teams, to Craig Tooley for his leadership of the LRO mission development team, and to Rich Burns and Steve Odendahl for their leadership of LRO mission operations. We are grateful to all of the LRO team members who contributed to the creation of the LRO Second Extended Science Mission proposal, which is the basis for much of this review. This paper is dedicated to the memory of Mike Wargo, whose enthusiastic support of LRO at NASA Headquarters showed that exploration and science can be highly successful partners.

## References

- Arnold, J.R., 1979. Ice in the lunar polar regions. *J. Geophys. Res.* 84, 5659–5668.
- Ashley, J.W., et al., 2012. Geology of the King Crater Region – New insights into impact melt dynamics on the Moon. *J. Geophys. Res.* 117, E00H29. doi:10.1029/2011JE003990.
- Aye, K.-M., et al., 2014. Diviner monitoring of coldest lunar polar regions. *Lunar Planet. Sci.* 45, 2893.
- Baker, D.M.H., Head, J.W., 2013. New morphometric measurements of craters and basins on Mercury and the Moon from MESSENGER and LRO altimetry and image data: An observational framework for evaluating models of peak-ring basin formation. *Planet. Space Sci.* 86, 91–116.
- Baker, D.M.H., et al., 2011. The transition from complex crater to peak-ring basin on the Moon: New observations from the Lunar Orbiter Laser Altimeter (LOLA) instrument. *Icarus* 214, 377–393.
- Baker, D.M.H., et al., 2012. The transition from complex craters to multi-ring basins on the Moon: Quantitative geometric properties from Lunar Reconnaissance Orbiter Lunar Orbiter Laser Altimeter (LOLA) data. *J. Geophys. Res.* 117, E00H16.
- Bandfield, J.L., et al., 2011. Lunar surface rock abundance and regolith fines temperatures derived from LRO Diviner Radiometer data. *J. Geophys. Res.* 116, E00H02.
- Bandfield, J.L., et al., 2014. Lunar cold spots: Granular flow features and extensive insulating materials surrounding young craters. *Icarus* 231, 221–231.
- Bandfield, J.L., et al., 2015. Lunar impact ejecta Strewen fields—Distal regions of oriented rocky deposits. *Lunar Planet. Sci.* 46, 1563.
- Banks, M.E., et al., 2012. Morphometric analysis of small-scale lobate scarps on the Moon using data from the Lunar Reconnaissance Orbiter. *J. Geophys. Res.* 117, E00H11.
- Bell, S.W., et al., 2012. Dating small fresh lunar craters with Mini-RF radar observations of ejecta blankets. *J. Geophys. Res.* 117, E00H30.
- Besserer, J., et al., 2014. GRAIL gravity constraints on the vertical and lateral density structure of the lunar crust. *Geophys. Res. Lett.* 41, 5771–5777.
- Bhattacharya, S., Chauhan, P., Ajai, 2013. Study of 2800-nm OH/H<sub>2</sub>O feature at Compton-Belkovich Thorium Anomaly (CBTA) in the far side of the Moon using Chandrayaan-1 Moon Mineralogy Mapper (M<sup>3</sup>) data. *Lunar Planet. Sci.* 44, 1382.
- Bleacher, L.V. et al., 2015. International observe the Moon night: An effective model for public engagement with NASA content. *Lunar Planet. Sci.* 46, 2281.
- Braden, S.E., Robinson, M.S., 2013. Relative rates of optical maturation of regolith on Mercury and the Moon. *J. Geophys. Res.: Planets* 118, 1903–1914.
- Braden, S.E., et al., 2014. Evidence for basaltic volcanism on the Moon within the past 100 million years. *Nat. Geosci.* 7, 787–791.
- Bray, V.J., et al., 2010. New insight into lunar impact melt mobility from the LRO camera. *Geophys. Res. Lett.* 37, L21202.
- Bruce Syal, M., Schultz, P.H., 2015. Cometary impact effects at the Moon: Implications for lunar swirl formation. *Icarus* 257, 194–206.
- Cahill, J.T.S., et al., 2014. The Miniature Radio Frequency instrument's (Mini-RF) global observations of Earth's Moon. *Icarus* 243, 173–190.
- Campbell, D.B., et al., 2006. No evidence for thick deposits of ice at the lunar south pole. *Nature* 443, 835–837.
- Carter, L.M., et al., 2012. Initial observations of lunar impact melts and ejecta flows with the Mini-RF radar. *J. Geophys. Res.* 117, E00H09.
- Case, A.W., et al., 2013. The deep space galactic cosmic ray lineal energy spectrum at solar minimum. *Space Weather* 11, 361–368.
- Chabot, N.L., et al., 2014. Images of surface volatiles in Mercury's polar craters acquired by the MESSENGER spacecraft. *Geology* 42, 1051–1054.
- Chin, G., et al., 2007. Lunar Reconnaissance Orbiter overview: The instrument suite and mission. *Space Sci. Rev.* 129, 391–419.
- Clark, R.N., 2009. Detection of adsorbed water and hydroxyl on the Moon. *Science* 326, 562–564.
- Colaprete, A., et al., 2010. Detection of water in the LCROSS ejecta plume. *Science* 330, 463–468.
- Cook, J.C., et al., 2013. New upper limits on numerous atmospheric species in the native lunar atmosphere. *Icarus* 225, 681–687.
- Crider, D.H., Vondrak, R.R., 2003. Space weathering effects on lunar cold trap deposits. *J. Geophys. Res.: Planets* 108, 5079.
- Daubar, I.J., et al., 2013. The current martian cratering rate. *Icarus* 225, 506–516.
- Denevi, B.W., et al., 2012. Physical constraints on impact melt properties from Lunar Reconnaissance Orbiter Camera images. *Icarus* 219, 665–675.
- Denevi, B.W., et al., 2014. Characterization of space weathering from Lunar Reconnaissance Orbiter Camera ultraviolet observations of the Moon. *J. Geophys. Res.: Planets* 119, 976–997.
- El-Baz, F., 1973. D-Caldera New Photographs of a Unique Feature. Apollo 17: Preliminary Science Report, vol. 330, pp. 30–13.
- Fassett, C.I., et al., 2011. Thickness of proximal ejecta from the Orientale Basin from Lunar Orbiter Laser Altimeter (LOLA) data: Implications for multi-ring basin formation. *Geophys. Res. Lett.* 38, L17201.
- Feldman, W.C., et al., 1998. Fluxes of fast and epithermal neutrons from Lunar Prospector: Evidence for water ice at the lunar poles. *Science* 281, 1496–1500.
- Feldman, W.C., et al., 2000. Polar hydrogen deposits on the Moon. *J. Geophys. Res.: Planets* 105, 4175–4195.
- Feldman, P.D., et al., 2012. Temporal variability of lunar exospheric helium during January 2012 from LRO/LAMP. *Icarus* 221, 854–858.
- Feldman, P.D., et al., 2014. Upper limits for a lunar dust exosphere from far-ultraviolet spectroscopy by LRO/LAMP. *Icarus* 233, 106–113.
- Garrick-Bethell, I., Head, J.W., Pieters, C.M., 2011. Spectral properties, magnetic fields, and dust transport at lunar swirls. *Icarus* 212, 480–492.
- Ghent, R.R., et al., 2014. Constraints on the recent rate of lunar ejecta breakdown and implications for crater ages. *Geology* 42, 1059–1062.
- Gladstone, G.R., et al., 2010. LRO-LAMP observations of the LCROSS impact plume. *Science* 330, 472–476.
- Gladstone, G.R., et al., 2010. LAMP: The Lyman Alpha Mapping Project on NASA's Lunar Reconnaissance Orbiter Mission. *Space Sci. Rev.* 150, 161–181.
- Glotch, T.D., et al., 2010. Highly silicic compositions on the Moon. *Science* 329, 1510–1513.
- Glotch, T.D., et al., 2011. The Mairan domes: Silicic volcanic constructs on the Moon. *Geophys. Res. Lett.* 38, L21204.
- Glotch, T.D., et al., 2015. Formation of lunar swirls by magnetic field standoff of the solar wind. *Nat. Commun.* 6, 1–8.
- Goswami, J.N., Lal, D., 1977. Particle track correlation studies in lunar soils: Long term fluctuations in ancient meteoritic flux in lunar space. *Lunar Planet. Sci.* 8, 368.
- Greenhagen, B.T., et al., 2010. Global silicate mineralogy of the Moon from the Diviner Lunar Radiometer. *Science* 329, 1507–1509.
- Greenhagen, B.T. et al., 2015. Using lunar eclipses to investigate the regolith boundary layer. *Lunar Planet. Sci.* 46, 2949.

- Gruener, J.E., Joosten, B.K., 2009. NASA Constellation Program office regions of interest on the Moon: A representative basis for scientific exploration, resource potential, and mission operations. *LPI Contributions* 1483, 50–51.
- Gustafson, J.O., et al., 2012. Characterization of previously unidentified lunar pyroclastic deposits using Lunar Reconnaissance Orbiter Camera data. *J. Geophys. Res.: Planets* 117, E00H25.
- Hapke, B., 2008. Bidirectional reflectance spectroscopy: 6. Effects of porosity. *Icarus* 195, 918–926.
- Hapke, B., Blewett, D., 1991. Coherent backscatter model for the unusual radar reflectivity of icy satellites. *Nature* 352, 46–47.
- Hapke, B., Nelson, R., Smythe, W., 1998. The opposition effect of the Moon: Coherent backscatter and shadow hiding. *Icarus* 133, 89–97.
- Haruyama, J., et al., 2008. Lack of exposed ice inside lunar south pole Shackleton crater. *Science* 322, 938–939.
- Haruyama, J., et al., 2009. Possible lunar lava tube skylight observed by SELENE cameras. *Geophys. Res. Lett.* 36, L21206.
- Hayne, P.O., et al., 2010. Diviner Lunar Radiometer observations of the LCROSS impact. *Science* 330, 477–479.
- Hayne, P., et al., 2013. Thermophysical properties of the lunar surface from diviner observations. *EGU General Assembly Conference Abstracts*, vol. 15, pp. 10871.
- Head, J.W., Gifford, A., 1980. Lunar mare domes – Classification and modes of origin. *Moon Planets* 22, 235–258.
- Head, J.W., et al., 2010. Global distribution of large lunar craters: Implications for resurfacing and impactor populations. *Science* 329, 1504–1507.
- Hendrix, A.R., et al., 2012. The lunar far-UV albedo: Indicator of hydration and weathering. *J. Geophys. Res.: Planets* 117, E12001.
- Hendrix, A.R., et al., 2012b. Far-ultraviolet characteristics of lunar swirls. *Lunar Planet. Sci.* 46, 2648 (abstracts).
- Hiesinger, H., et al., 2012. How old are young lunar craters? *J. Geophys. Res.* 117, E00H10.
- Hodges, C.A. et al., 1973. Geologic setting of Apollo 16. *Proc. Lunar Sci. Conf.* 4, 1–25.
- Hoffman, J.H. et al., 1973. Lunar atmospheric composition results from Apollo 17. *Proc. Lunar Sci. Conf.* 4, 2865–2875.
- Hurley, D.M., et al., 2012. Modeling of the vapor release from the LCROSS impact: 2. Observations from LAMP. *J. Geophys. Res.* 117, E00H07.
- Jolliff, B., et al., 2000. Major lunar crustal terranes: Surface expressions and crust–mantle origins. *J. Geophys. Res.* 105, 4197–4216.
- Jolliff, B.L., et al., 2010. Imaging Constellation regions of interest with the Lunar Reconnaissance Orbiter Cameras. *LPI Contributions* 1595, 32.
- Jolliff, B.L., et al., 2011. Non-mare silicic volcanism on the lunar farside at Compton–Belkovich. *Nat. Geosci.* 4, 566–571.
- Jones, A.J.P. et al., 2015. LRO's lunar workshops for educators: A proven model of exceptional professional development for teachers. *Lunar Planet. Sci.* 46, 1898.
- Jordan, A. et al., 2012. Deep dielectric charging of the Moon. *American Geophysical Union (Fall)*. Abstracts 53, 2054.
- Jordan, A.P., et al., 2013. The formation of molecular hydrogen from water ice in the lunar regolith by energetic charged particles. *J. Geophys. Res.: Planets* 118, 1257–1264.
- Kadish, S.J. et al., 2011. A global catalog of large lunar craters (>20 km) from the Lunar Orbiter Laser Altimeter. *Lunar Planet. Sci.* 42, 1006 (abstracts).
- Khan, A., Mosegaard, K., 2005. Further constraints on the deep lunar interior. *Geophys. Res. Lett.* 32, L22203.
- Kirchoff, M.R., et al., 2013. Ages of large lunar impact craters and implications for bombardment during the Moon's middle age. *Icarus* 225, 325–341.
- Kramer, G.Y., et al., 2013. Spectral and photogeologic mapping of Schrödinger basin and implications for post-South Pole-Aitken impact deep subsurface stratigraphy. *Icarus* 223, 131–148.
- Kreslavsky, M.A., et al., 2013. Lunar topographic roughness maps from Lunar Orbiter Laser Altimeter (LOLA) data: Scale dependence and correlation with geologic features and units. *Icarus* 226, 52–66.
- Lachenbruch, A.H., 1968. Discussion of the paper by Kenneth Watson, 'Proposed lunar heat flow measurement from a polar orbiting satellite'. *J. Geophys. Res.* 73, 822–823.
- Lawrence, D.J., et al., 2003. Small-area thorium features on the lunar surface. *J. Geophys. Res.: Planets* 108 (E9), 5102. doi:10.1029/2003JE002050.
- Lawrence, S.J., et al., 2010. LROC views the Constellation regions of interest: Science and exploration observations. *LPI Contributions* 1595, 35.
- Lawrence, S.J., et al., 2013. LRO observations of morphology and surface roughness of volcanic cones and lobate lava flows in the Marius Hills. *J. Geophys. Res.: Planets* 118, 615–634.
- Little, R.C. et al., 2000. Temperature dependence of thermal neutrons from the Moon. In: *6th Radiation Protection and Shielding Topical Conference*, pp. 463–469.
- Livengood, T.A., et al., 2015. Moonshine: Diurnally varying hydration through natural distillation on the Moon, detected by the Lunar Exploration Neutron Detector (LEND). *Icarus* 255, 100–115.
- Looper, M.D., et al., 2013. The radiation environment near the lunar surface: CRaTER observations and Geant4 simulations. *Space Weather* 11, 142–152.
- LROC Team, Malaret, E., Battisti, A., 2015. LROC QuickMap.
- Mazarico, E., et al., 2011. Illumination conditions of the lunar polar regions using LOLA topography. *Icarus* 211, 1066–1081.
- Mazarico, E.M., et al., 2014. Detection of the lunar body tide by the Lunar Orbiter Laser Altimeter. *Geophys. Res. Lett.* 41 (7), 2282–2288. doi:10.1002/2013GL059085.
- McClanahan, T.P., et al., 2015. Evidence for the sequestration of hydrogen-bearing volatiles towards the Moon's southern pole-facing slopes. *Icarus* 255, 88–99.
- Mendell, W., 2010. Foreword: An exploration-driven renaissance in lunar science. *Space Sci. Rev.* 150, 3–6.
- Mitrofanov, I.G., et al., 2010. Lunar Exploration Neutron Detector for the NASA Lunar Reconnaissance Orbiter. *Space Sci. Rev.* 150, 183–207.
- Mitrofanov, I.G., et al., 2010. Hydrogen mapping of the lunar south pole using the LRO neutron detector experiment LEND. *Science* 330, 483–486.
- Mitrofanov, I., et al., 2012. Testing polar spots of water-rich permafrost on the Moon: LEND observations onboard LRO. *J. Geophys. Res.: Planets* 117, E00H27.
- Morbidelli, A., et al., 2012. A sawtooth-like timeline for the first billion years of lunar bombardment. *Earth Planet. Sci. Lett.* 355–356, 144–151.
- Morgan, T.H., Shemansky, D.E., 1991. Limits to the lunar atmosphere. *J. Geophys. Res.* 96, 1351–1367.
- Moses, J.I., et al., 1999. External sources of water for Mercury's putative ice deposits. *Icarus* 137, 197–221.
- Nahm, A.L., Öhman, T., Kring, D.A., 2013. Normal faulting origin for the Cordillera and Outer Rook Rings of Orientale Basin, the Moon. *J. Geophys. Res.: Planets* 118, 190–205.
- Neish, C.D., et al., 2011. The surficial nature of lunar swirls as revealed by the Mini-RF instrument. *Icarus* 215, 186–196.
- Neish, C.D. et al., 2011b. Correlation between surface roughness and slope on a lunar impact melt. *Lunar Planet. Sci.* 42, 1881.
- Nelson, R.M., et al., 2000. The opposition effect in simulated planetary regoliths. Reflectance and Circular Polarization Ratio change at small phase angle. *Icarus* 147, 545–558.
- Neukum, G., Ivanov, B.A., 1994. Crater size distributions and impact probabilities on Earth from lunar, terrestrial-planet, and asteroid cratering data. In: Gehrels, T. (Ed.), *Hazards Due to Comets and Asteroids*, pp. 359.
- Neukum, G., Ivanov, B.A., Hartmann, W.K., 2001. Cratering records in the inner Solar System in relation to the lunar reference system. *Space Sci. Rev.* 96, 55–86.
- Nozette, S., et al., 2010. The Lunar Reconnaissance Orbiter Miniature Radio Frequency (Mini-RF) technology demonstration. *Space Sci. Rev.* 150, 285–302.
- Paige, D.A., et al., 2010. The Lunar Reconnaissance Orbiter Diviner Lunar Radiometer Experiment. *Space Sci. Rev.* 150, 125–160.
- Paige, D.A., et al., 2010. Diviner Lunar Radiometer observations of cold traps in the Moon's south polar region. *Science* 330, 479–482.
- Paige, D.A., et al., 2013. Thermal stability of volatiles in the north polar region of Mercury. *Science* 339, 300–303.
- Paige, D.A. et al., 2015. Lunar surface properties from new Diviner eclipse observations. *Lunar Planet. Sci.* 46, 2953.
- Patterson, G.W., et al., 2014. Mini-RF bistatic observations of Cabeus crater. *LPI Contributions* 1820, 3049.
- Pepin, R.O. et al., 1974. Rare gases and trace elements in Apollo 15 drill core fines depositional chronologies and K–Ar ages, and production rates of spallation-produced He-3, Ne-21, and Ar-38 versus depth. *Proc. Lunar Sci. Conf.* 5, 2149–2184.
- Petro, N.E. et al., 2013. Presence of OH/H<sub>2</sub>O associated with the Lunar Compton–Belkovich Volcanic Complex identified by the Moon Mineralogy Mapper (M<sup>3</sup>). *Lunar Planet. Sci.* 44, 2688.
- Piatek, J.L., et al., 2004. Scattering properties of planetary regolith analogs. *Icarus* 171, 531–545.
- Pieters, C.M., et al., 2009. Character and spatial distribution of OH/H<sub>2</sub>O on the surface of the Moon seen by M-3 on Chandrayaan-1. *Science* 326, 568–572.
- Retherford, K.D. et al., 2013. LRO-Lyman Alpha Mapping Project (LAMP) observations of the GRAIL impacts. *Lunar Planet. Sci.* 44, 3004.
- Robinson, M.S., et al., 2010. Lunar Reconnaissance Orbiter Camera (LROC) instrument overview. *Space Sci. Rev.* 150, 81–124.
- Robinson, M.S., et al., 2012. Confirmation of sublunarean voids and thin layering in mare deposits. *Planet. Space Sci.* 69, 18–27.
- Robinson, M.S., et al., 2015. New crater on the Moon and a swarm of secondaries. *Icarus* 252, 229–235.
- Rosenburg, M.A., et al., 2011. Global surface slopes and roughness of the Moon from the Lunar Orbiter Laser Altimeter. *J. Geophys. Res.: Planets* 116, E02001.
- Rosenburg, M.A., Aharonson, O., Sari, R.E., 2015. Topographic power spectra of cratered terrains: Theory and application to the Moon. *J. Geophys. Res.: Planets* E004746.
- Saal, A.E., et al., 2008. Volatile content of lunar volcanic glasses and the presence of water in the Moon's interior. *Nature* 454, 192–195.
- Sanin, A.B., et al., 2012. Testing lunar permanently shadowed regions for water ice: LEND results from LRO. *J. Geophys. Res.: Planets* 117, E00H26.
- Sato, H., et al., 2014. Resolved Hapke parameter maps of the Moon. *J. Geophys. Res.: Planets* 119, 1775–1805.
- Schorghofer, N., Taylor, G.J., 2007. Subsurface migration of H<sub>2</sub>O at lunar cold traps. *J. Geophys. Res.: Planets* 112, E02010.
- Schwadron, N.A., Spence, H.E., Came, R., 2011. Does the space environment affect the ecosphere? *Eos, Trans. Am. Geophys. Union* 92, 297–298.
- Schwadron, N.A., et al., 2012. Lunar radiation environment and space weathering from the Cosmic Ray Telescope for the Effects of Radiation (CRaTER). *J. Geophys. Res.: Planets* 117, E00H13.
- Schwadron, N.A., Smith, S., Spence, H.E., 2013. The CRaTER special issue of *Space Weather: Building the observational foundation to deduce biological effects of space radiation*. *Space Weather* 11, 47–48.
- Schwadron, N.A., et al., 2014. Does the worsening galactic cosmic radiation environment observed by CRaTER preclude future manned deep space exploration? *Space Weather* 12, 622–632.
- Shoemaker, E.M., 1962. Interpretation of lunar craters. In: Kopal, Z. (Ed.), *Physics and Astronomy of the Moon*. Academic Press, New York, pp. 277–339.

- Siegler, M.A., Smrekar, S.E., 2014. Lunar heat flow: Regional perspective of the Apollo landing sites. *J. Geophys. Res.: Planets* 119, 47–63.
- Siegler, M.A., Bills, B.G., Paige, D.A., 2011. Effects of orbital evolution on lunar ice stability. *J. Geophys. Res.: Planets* 116, E03010.
- Siegler, M.A. et al., 2012. Lunar heat flow: A global perspective. *American Geophysical Union (Fall). Abstracts* 52, 08.
- Siegler, M.A. et al., 2013. Crustal effects on lunar heat flow. *Lunar Planet. Sci.* 44, 2516.
- Siegler, M., et al., 2015. Evolution of lunar polar ice stability. *Icarus* 255, 78–87.
- Smith, D.E., et al., 2010. The Lunar Orbiter Laser Altimeter investigation on the Lunar Reconnaissance Orbiter Mission. *Space Sci. Rev.* 150, 209–241.
- Spence, H.E., et al., 2010. CRaTER: The Cosmic Ray Telescope for the Effects of Radiation experiment on the Lunar Reconnaissance Orbiter Mission. *Space Sci. Rev.* 150, 243–284.
- Speyerer, E.J., Robinson, M.S., 2013. Persistently illuminated regions at the lunar poles: Ideal sites for future exploration. *Icarus* 222, 122–136.
- Spudis, P.D., et al., 2010. Initial results for the north pole of the Moon from Mini-SAR, Chandrayaan-1 mission. *Geophys. Res. Lett.* 37 (6). doi:10.1029/2009GL042259.
- Spudis, P.D., et al., 2013. Evidence for water ice on the Moon: Results for anomalous polar craters from the LRO Mini-RF imaging radar. *J. Geophys. Res.: Planets* doi:10.1002/jgre.20156, 2012JE004312.
- Spudis, P.D., McGovern, P.J., Kiefer, W.S., 2013. Large shield volcanoes on the Moon. *J. Geophys. Res.: Planets* 118, 1063–1081.
- Stern, S.A., et al., 2012. Lunar atmospheric helium detections by the LAMP UV spectrograph on the Lunar Reconnaissance Orbiter. *Geophys. Res. Lett.* 39, L12202.
- Stern, S.A., et al., 2013. Lunar atmospheric H<sub>2</sub> detections by the LAMP UV spectrograph on the Lunar Reconnaissance Orbiter. *Icarus* 226, 1210–1213.
- Stopar, J.D., et al., 2014. Occurrence and mechanisms of impact melt emplacement at small lunar craters. *Icarus* 243, 337–357.
- Suggs, R.M., et al., 2014. The flux of kilogram-sized meteoroids from lunar impact monitoring. *Icarus* 238, 23–36.
- Sunshine, J.M., et al., 2009. Temporal and spatial variability of lunar hydration as observed by the Deep Impact spacecraft. *Science* 326, 565–568.
- Teodoro, L.F.A., et al., 2014. How well do we know the polar hydrogen distribution on the Moon? *J. Geophys. Res.* 119, 574–593.
- Tomson Jones, J., Kekesi, A., Estrada, L., 2015. NASA Goddard Scientific Visualization Studio.
- Tooley, C.R., et al., 2010. Lunar Reconnaissance Orbiter Mission and spacecraft design. *Space Sci. Rev.* 150, 23–62.
- Vasavada, A.R., et al., 2012. Lunar equatorial surface temperatures and regolith properties from the Diviner Lunar Radiometer Experiment. *J. Geophys. Res.* 117, E00H18.
- Vondrak, R., et al., 2010. Lunar Reconnaissance Orbiter (LRO): Observations for lunar exploration and science. *Space Sci. Rev.* 150, 7–22.
- Wagner, R.V., Robinson, M.S., 2014. Distribution, formation mechanisms, and significance of lunar pits. *Icarus* 237, 52–60.
- Watson, K., Brown, H., Murray, B., 1961. On the possible presence of ice on Moon. *J. Geophys. Res.* 66, 1598–1600.
- Watters, T.R., et al., 2010. Evidence of recent thrust faulting on the Moon revealed by the Lunar Reconnaissance Orbiter Camera. *Science* 329, 936–940.
- Watters, T.R., et al., 2012. Recent extensional tectonics on the Moon revealed by the Lunar Reconnaissance Orbiter Camera. *Nat. Geosci.* 5, 181–185.
- Watters, T.R., et al., 2015. Global thrust faulting on the Moon and the influence of tidal stresses. *Geology* 43, 851–854.
- Whitaker, E.A., 1972. An Unusual Mare Feature. *Apollo 15: Preliminary Science Report*, vol. 289, pp. 84.
- Whitten, J.L., Head III, J.W., 2013. Detecting volcanic resurfacing of heavily cratered terrain: Flooding simulations on the Moon using Lunar Orbiter Laser Altimeter (LOLA) data. *Planet. Space Sci.* 85, 24–37.
- Williams, J.G., 2008. Lunar core and mantle. What does LLR see? In: 16th International Workshop on Laser Ranging, pp. 17.
- Williams, J.G., Boggs, D.H., Ratcliff, J.T., 2013. Lunar science from lunar laser ranging. *Lunar Planet. Sci.* 44, 2377.
- Williams, J.-P., Paige, D.A., Jögi, P., 2015. Impact melt deposits at the antipodes of Tycho and Copernicus craters. *Lunar Planet. Sci.* 46, 2738.
- Wilson, J.K., et al., 2012. The first cosmic ray albedo proton map of the Moon. *J. Geophys. Res.* E00H23.
- Wilson, J.K. et al., 2015a. Lunar proton albedo anomalies: Soil, surveyors, and statistics. *Lunar Planet. Sci.* 46, 2229.
- Wilson, J.T., et al., 2015. Evidence for explosive silicic volcanism on the Moon from the extended distribution of thorium near the Compton–Belkovich Volcanic Complex. *J. Geophys. Res.: Planets* 120, 92–108.
- Wöhler, C., Lena, R., Phillips, J., 2007. Formation of lunar mare domes along crustal fractures: Rheologic conditions, dimensions of feeder dikes, and the role of magma evolution. *Icarus* 189, 279–307.
- Zuber, M.T., et al., 2010. The Lunar Reconnaissance Orbiter laser ranging investigation. *Space Sci. Rev.* 150, 63–80.
- Zuber, M.T., et al., 2012. Constraints on the volatile distribution within Shackleton crater at the lunar south pole. *Nature* 486, 378–381.